ELECTRON ENERGY DISTRIBUTION MEASUREMENTS IN THE PLUME REGION OF A LOW CURRENT HOLLOW CATHODE

by

Nicholas James Behlman

A Thesis

Submitted to the Faculty

of the

WORCESTER POLYTECHNIC INSTITUTE

in partial fulfillment of the requirements of the

Degree of Master of Science

in

Mechanical Engineering

December 2009

APPROVED:

Dr. John J. Blandino, Advisor
Associate Professor, Mechanical Engineering Department

Dr. Nikolaos A. Gatsonis, Committee Member
Professor, Mechanical Engineering Department

Dr. Islam I. Hussein, Committee Member
Assistant Professor, Mechanical Engineering Department

Mr. Bruce Pote, Committee Member
Busek Co. Inc., Natick, MA

Dr. Mark W. Richman, Graduate Committee Representative
Associate Professor, Mechanical Engineering Department

Abstract

A hollow cathode is an electron source used in a number of different electric thrusters for space propulsion. One important component of the device that helps initiate and sustain the discharge is called the keeper electrode. Cathode keeper erosion is one of the main limiting factors in the lifetime of electric thrusters. Sputtering due to high-energy ion bombardment is believed to be responsible for keeper erosion. Existing models of the cathode plume, including the OrCa2D code developed at Jet Propulsion Laboratory, do not predict these high-energy ions and experimental measurement of the electron energy distribution function (EEDF) could provide useful information for the development of a high fidelity model of the plume region. Understanding of the mechanism by which these high-energy ions are produced could lead to improvements in the design of hollow cathodes.

The primary focus of this work is to determine the EEDF in the cathode plume. A single Langmuir probe is used to measure the current-voltage (I-V) characteristic of the plasma plume from a low current hollow cathode in the region downstream of the keeper orifice. The EEDF is obtained using the Druyvesteyn procedure (based on interpretation of the second derivative of the I-V curve), and parameters such as electron temperature, plasma density and plasma potential are also obtained. The dependence of the EEDF and other parameters on the radial position in the plume is examined. Results show that the EEDF deviates from the Maxwellian distribution, and is more accurately described by the Druyvesteyn distribution directly downstream of the cathode. Off-axis measurements of the EEDF indicate the presence of fast electrons, most likely due to the anode geometry. The cathode used in these tests is representative of the cathode used in a 200W class Hall thruster. Data is presented for a hollow cathode operating on argon gas for two cases with different discharge currents.

To my grandfather, Rudolph James Russo, who encouraged me to "stay on it."

Acknowledgements

It is my pleasure to recognize the people who have made this work possible.

Professor John J. Blandino for his direction and guidance throughout my time at WPI. Professor Blandino's door is always open, and I thank him for investing his time in my education.

Professor Nikolaos A. Gatsonis who has opened other research opportunities for me and provided guidance in those endeavors.

Busek Co. Inc. in Natick, MA who provided the hollow cathode used in the experiment. In particular, thanks to Bruce Pote and Chas Freeman for making available other materials and equipment and troubleshooting the gas feed system and cathode itself.

Neil Whitehouse for his patience and expertise in the machine shop, Barbara Furhman for her timely processing of a steady stream of purchase orders, and Daniel Asselin for his assistance and problem solving skills.

WPI and the Mechanical Engineering Department in particular for their support through the teaching assistantship program.

I have been fortunate to have the lifelong support of my family and friends. I owe my deepest gratitude to my mother, Mary Ellen Behlman, and my brother Trevor Behlman as well as my grandfather and grandmother Rudolph and Helen Russo who put WPI within my reach.

Contents

List of Figures

List of Tables

Nomenclature

Γ	Flux
γ	Specific heat ratio
ϵ	Energy
ε	Permittivity of free space
λ	Mean free path
λ_D	Debye length
λ_e	Electron mean free path
λ_i	Ion mean free path
λ_n	Neutral mean free path
μ	Reduced mass
σ_m	Momentum transfer cross section
τ_l	End effect parameter
ϕ_p	Plasma potential
χ	Scattering angle
$\chi(C)$	Speed distribution function
a	Speed of sound
A_p	Surface area of probe
A_s	Surface area of sheath
C	Speed
c	Exhaust velocity
C_i	Velocity component, Bohm velocity
d_p	Probe diameter
d_{ph}	Probe holder diameter
e	Elementary charge
$F(\epsilon)$	Electron energy distribution function

$f(\epsilon)$	Normalized electron energy distribution function
$F(C_i)$	Velocity distribution function
$f(C_i)$	Normalized velocity distribution function
g	Relative velocity
g_o	Acceleration due to gravity
h	Angular momentum, critical impact parameter
I	Current
I_t	Total impulse
I_{se}	Electron saturation current
I_{si}	Ion saturation current
I_{sp}	Specific impulse
J	Electron current density
k	Boltzmann constant
K_n	Knudsen number
L	Characteristic length
l_p	Probe length
m	Mass
m_e	Mass of electron
m_i	Mass of ion
m_o	Initial spacecraft mass
m_p	Propellant mass
N	Number of particles
n	Number density
n_e	Electron number density
n_i	Ion number density
q	Charge

R	Gas constant
r_m	Distance of closest approach
r_p	Probe radius
T	Temperature
T_e	Electron temperature
T_i	Ion temperature
V	Voltage
v	Velocity
V_C	Velocity space
V_p	Probe voltage
v_{th}	Thermal velocity

1 Introduction

1.1 Electric Propulsion

Rockets generate thrust by ejecting mass at high velocity. By Newton's second law, the time rate of change in momentum results in a force imparted on the vehicle. The thrust generated by a rocket is proportional to the exhaust velocity and rate at which mass is ejected.

$$F = \dot{m}c \tag{1}$$

The change in velocity that can be achieved is related to the mass fraction of propellant and the exhaust velocity.

$$\Delta V = c \ln\left(\frac{m_o}{m_o - m_p}\right) \tag{2}$$

Using more propellant to improve the ΔV capability of the rocket gives diminishing returns. Adding more propellant increases the mass of the spacecraft, which increases the amount of propellant needed. For a fixed exhaust velocity, achieving a high ΔV comes at the expense of a high propellant mass fraction. Increasing the exhaust velocity does not drive the mass of the spacecraft in this way.

Specific impulse, I_{sp}, is a measure of the efficiency of propellant use. It is equal to the total amount of impulse delivered to the spacecraft divided by the weight of the propellant consumed.

$$I_{sp} = \frac{I_t}{m_p g_o} = \frac{c}{g_o} \tag{3}$$

It is not surprising that the specific impulse is directly related to the exhaust velocity. The only way to get more impulse from a fixed amount of ejected mass is to increase the velocity at which it is ejected. In chemical rockets, the exhaust velocity, and consequently the specific impulse are limited by the physics of the expansion of the gas. Electric propulsion devices

are capable of achieving much higher specific impulses than chemical rockets. Table 1 and Figure 1 compare performance values for different rocket technologies.

Engine Type	I_{sp} (sec)	c (m/sec)	$\dot{m}$ (kg/sec)	Power Input (kW)
Chemical rocket	300	2940	0.0340	294
Nuclear fission	800	7840	0.0128	787
Arc-electrothermal	600	5880	0.170	588
Ion electrostatic	2000	19,600	0.0051	1959

Table 1: Typical Performance Values for Different Engine Types[1]

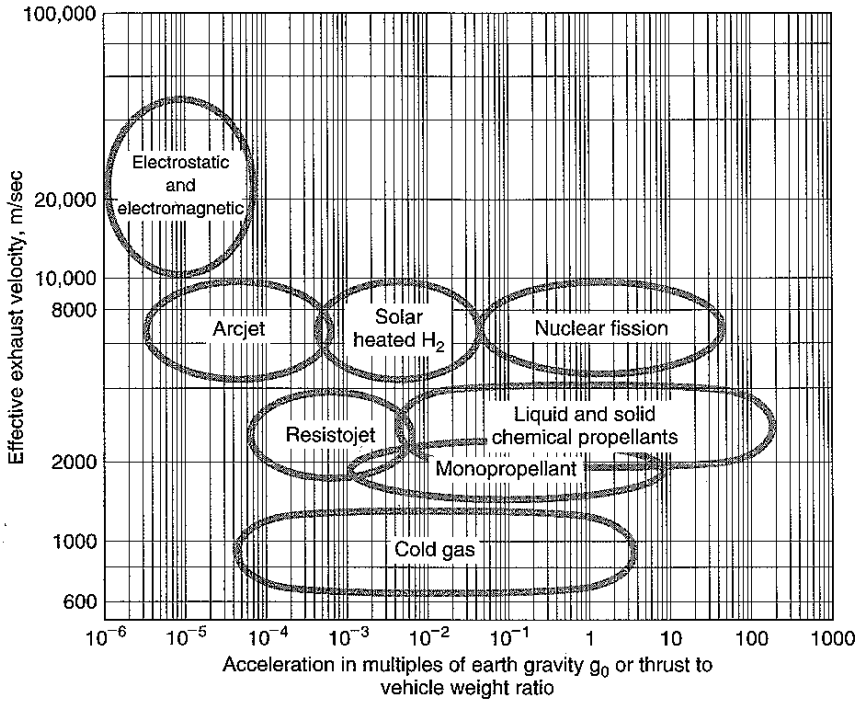

Figure 1: Exhaust Velocities and Thrust Capabilities of Various Rocket Technologies[1]

In electric thrusters, the utilization of an energy source that is independent of the propellant relieves the upper limit imposed on the I_{sp} by the dynamics of chemical rockets. The increased specific impulse reduces the propellant mass ratio, thereby reducing the overall

size and mass of the spacecraft. The performance of a spacecraft can be improved to a point by increasing the I_{sp} with additional electrical power, however the additional mass of the power supply mass can become a significant fraction of the total spacecraft mass. Therefore, there is an optimum I_{sp} for an electric propulsion spacecraft. Electric thrusters are the only feasible option for many high ΔV missions, where maximizing the payload mass fraction is critical. Ion and Hall thrusters are examples of electrostatic thrusters, the most common electric propulsion technology.

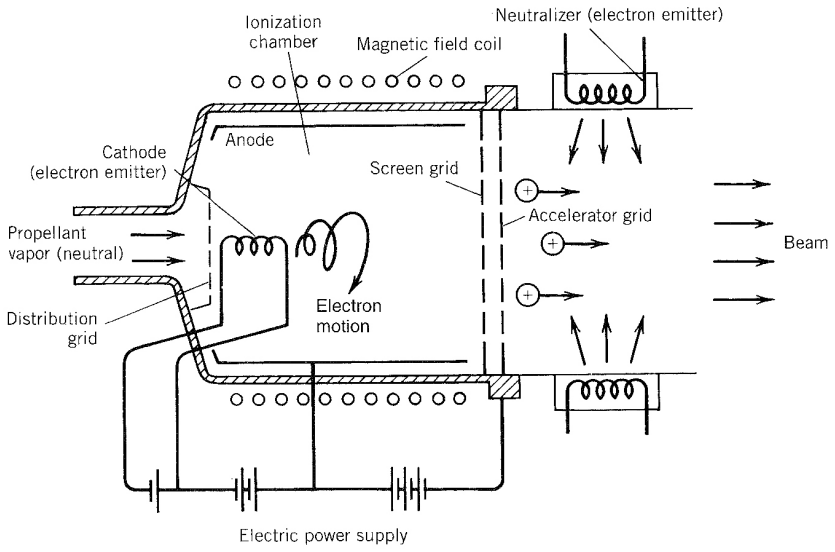

Figure 2: Functional Diagram of Ion Thruster[1]

An ion thruster accelerates charged particles electrostatically through a set of electrodes or grids.[1] Electrons are emitted from a hollow cathode inside the ionization chamber called the discharge cathode assembly (DCA). A neutral gas flows into the chamber where it is ionized by electron bombardment. A cylindrical anode near the wall of the ionization chamber draws electrons out of the chamber, and magnets around the chamber cause the electrons to travel in a helical pattern to maximize the number of ionizing collisions with the neutral gas. An axial potential gradient forces the ions downstream towards an accelerator grid. Ions are electrostatically accelerated through the grid to produce thrust. A second cathode

then neutralizes the plume from the thruster to ensure that the spacecraft remains charge neutral. This avoids the possibility of coulomb attraction between the spacecraft and the plume.

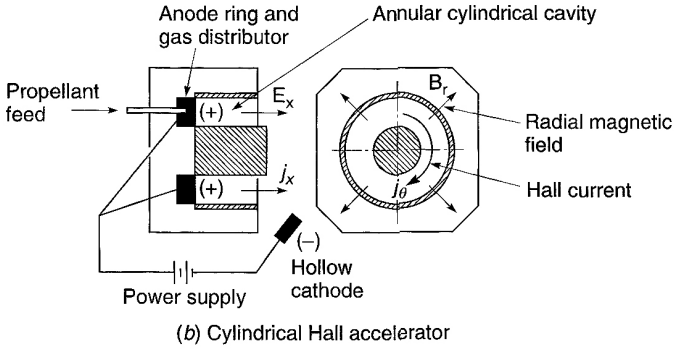

Figure 3: Functional Diagram of Hall Thruster[1]

A Hall thruster is another example of an electrostatic thruster. An electric field is applied in the axial direction, and a magnetic field is applied in the radial direction. This gives rise to a Hall current and electron flux in the azimuthal direction. This is called the Hall effect, and it is used to trap electrons in a swirling motion around a cylindrical cavity. Neutral gas is injected into the cavity and ionized by the constrained electrons. Ions are accelerated through an axial electric field resulting from electron density gradient created by the Hall effect.[2] As with an ion thruster, the plume of ejected ions must be neutralized to prevent the beam of ions from being drawn back towards the spacecraft. A hollow cathode (described in Section 1.3) is typically used for this purpose.

Ion and Hall thrusters both have a very high specific impulse, but are also characterized by their low thrust output. As a result, the required thrust time necessary to achieve a specified ΔV is typically large (on the order of months in some cases). Component reliability is therefore a key area of interest for these long duration missions.

1.2 Plasma Parameters

A plasma can be loosely defined as an ionized gas. Atoms in a plasma dissociate into ions and electrons, and the physics that govern the behavior of a plasma involve Coulomb collisions as well as ionization and charge-exchange collisions. Chen[10] offers a more specific definition.

> A plasma is a quasineutral gas of charged and neutral particles which exhibits collective behavior.

The term "collective behavior" has to do with the long-range effects of the Coulomb force. The behavior of air at room temperature is driven by collisions. Information in one region is propagated throughout the gas by a cascade of collisions. In a plasma, forces can be exerted over a longer range, therefore an element of plasma has an effect on more than just its immediate neighbors, and the overall behavior can be described as "collective." The concept of quasineutrality is the condition that although ions and electrons move freely in a plasma, the density of the plasma over a volume with length scale greater than the Debye length can still be defined as a single quantity n, the plasma density.[10]

$$n_i \approx n_e \approx n \tag{4}$$

A Debye length is characteristic length over which a significant charge gradient can exist in a plasma. In a plasma, a sheath will form around a charged body that effectively insulates the region near the body from the rest of the plasma. This effect is called Debye shielding and the Debye length is related to the thickness of the sheath.[10] The mathematical definition is a function of electron temperature and electron density.

$$\lambda_D = \sqrt{\frac{\varepsilon_0 T_e}{n_e e}} \tag{5}$$

The condition of quasineutrality can also be defined as the condition in which the Debye length is much smaller than the dimensions of the system.

$$\lambda_D \ll L \tag{6}$$

This condition is a requirement for a gas to be designated as a plasma. The Debye shielding phenomenon is important in the theory of Langmuir probes because a sheath forms around the probe. It is necessary to understand the sheath in order to characterize the surrounding plasma outside the sheath.

1.3 Hollow Cathodes

1.3.1 Theory of Operation

The hollow cathode provides a source of electrons to neutralize the plasma plume from an ion or Hall thruster. Figure 4 provides a functional diagram of a hollow cathode. Electrons are produced by thermionic emission from a low-work-function insert. An inert gas such as argon or xenon flows through the cathode tube and is ionized in the insert region. The keeper electrode surrounds the cathode tube and is biased positive relative to the cathode tube. The electric field accelerates electrons through the cathode orifice toward the keeper. If the space potential outside the keeper is above the cathode potential, electrons are then accelerated through the keeper orifice into the thruster plume. As the neutral gas exits the cathode, it expands and is largely collisionless in the plume region.[2]

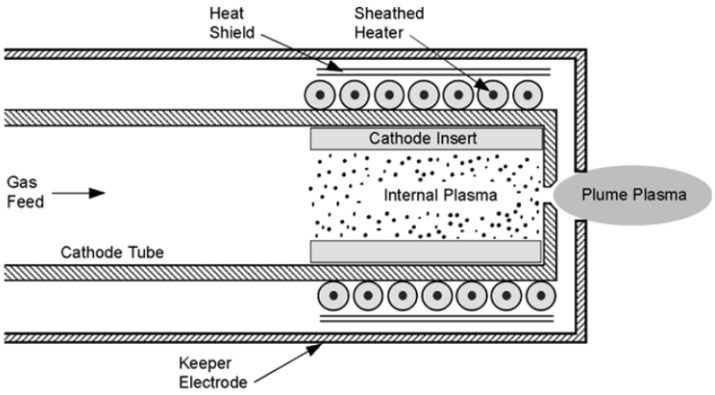

Figure 4: Cross-sectional Diagram of a Hollow Cathode[2]

1.3.2 Review of Prior Work

The Jet Propulsion Laboratory conducted an extended life test of the NASA Solar Electric Propulsion Technology Application Readiness (NSTAR) ion engine. After 30,000 hours of operation, the downstream face of the the keeper electrode on the discharge cathode was completely eroded away.[11] High-energy ion bombardment is believed to be responsible for keeper erosion.[12,9,4,13] The source of these high-energy ions remains largely unexplained.

It has been suggested that high-energy ions just downstream of the keeper orifice arise from the formation of a double layer in the plume region. A double layer, or double sheath, is an interface between a region of high local electron density and a region of high local ion density. The local electric field is strong between the two regions, and the potential changes sharply. This can either reflect or accelerate charged particles that enter the potential gradient.[14] Experimental data presented by Katz[3] predicts a steep gradient in the plasma potential in the near-orifice region of the plume when the gas flow rate is on the order or 5 sccm. This could be a source of high energy ions that erode the keeper. It has also been suggested that the steep rise in potential can occur in the keeper orifice, causing energetic ions to erode and enlarge the orifice via sputtering. Katz[3] also presents a one-

dimensional model based on the ambipolar diffusion equation, Ohm's law, and conservation of electron energy. The density of neutral particles is assumed to decrease exponentially with increasing axial distance from the cathode. Figure 5 shows the axial variation of the plasma potential predicted by the model compared with experiment. There is a sudden rise in the experimentally determined plasma potential approximately 15 cm downstream of the keeper.

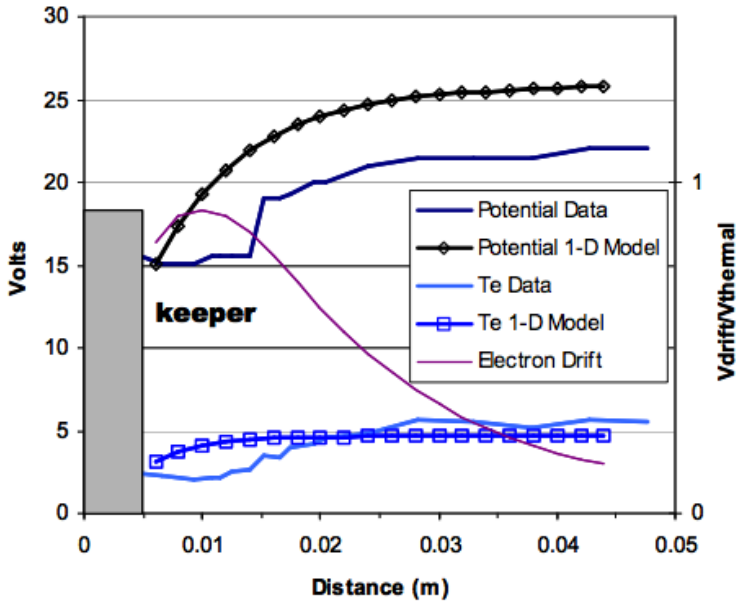

Figure 5: Model Predictions and Experimental Data in Plume Region[3]

Katz[3] concludes that the one-dimensional model used is too simple to describe the plume. As the flow rate is increased the model suggests that the double layer disappears, however a dip in density that is characteristic of a double layer is still visible in the plume. It is suspected that the model is not valid for higher flow rates.

Figure 6: Cathode Spot at 5.5 sccm (left) and 10 sccm (right)[3]

Williams *et al.*[15] measured keeper erosion rates during cathode operation. The density of the sputtered molybdenum was determined through laser-induced fluorescence (LIF), and used to calculate the erosion rate. Regions of high molybdenum density were consistent with areas erosion identified in the JPL Extended Life Test. Four beam-LIF was used to measure the velocities of xenon ions in all directions, and generate the velocity distribution of the ions. Tests were run with and without a keeper electrode. The results showed that the keeper electrode was effective in reducing the plasma density near the cathode, but had only a marginal effect on the velocity distribution of xeon ions. In both cases, a potential hill was observed downstream of the orifice of the discharge cathode assembly (DCA). These findings appear to be consistent with the one-dimensional model developed by Katz.[3] In the test with the keeper electrode, the potential hill was located approximately one centimeter from the orifice. The magnitude of the potential hill was directly related to the discharge voltage and current. A larger potential hill causes a greater component of back-flowing ions, which are responsible for erosion of the keeper.

Other tests have been unable to verify the existence of a potential hill in the plume. Goebel *et al.*[9] used an ultra-fast miniature scanning probe to interrogate the plasma potential distribution as unobtrusively as possible. A potential hill was detected in the 10 sccm test, but not in the 5.5 sccm case. In both cases a bright cathode spot is visible, however this is not necessarily the result of a double layer. The measured discontinuity in plasma potential

occurs at the downstream edge of the spot in the 10 sccm test. This is not the case with the 5.5 sccm test, making it less likely that the visual boundary corresponds to a double layer. The authors conclude that there was no potential hill strong enough to be the cause of the high-energy ions that could erode the keeper. It is also suggested that the cathode tested had too large an orifice, and therefore too low a current density to generate a large potential hill.

Experiments at the Jet Propulsion Laboratory (JPL) on the Nuclear Electric Xenon Ion System (NEXIS) and NSTAR cathodes determined that there is no DC potential hill near the cathode orifice.[12] An array of three scanning probes were used to generate distributions of the plasma potential in the axial and radial directions, while a retarding potential analyzer (RPA) was used to detect high-energy ions. Very few high-energy ions were detected downstream of the cathode on axis, however there was a significant number of high-energy ions moving in the radial direction.[4] Figure 7 shows the energy distribution of ions near the orifice moving in both the radial and axial direction. These were obtained by positioning the RPA radially or axially downstream of the cathode orifice. The discharge voltage V_d is indicated by a vertical line. The energy distribution for ions traveling in the radial direction is almost entirely above the discharge voltage.

It is expected that these ions have at least some small axial component, allowing them to impact and damage the keeper. Only a very small amount of ions located on-axis had energies exceeding the discharge voltage. The high-energy ions appear to be focused near the keeper and traveling mostly in the radial direction. These JPL tests found no electrostatic potential mechanism for the acceleration of these ions to such high speeds, however RF instabilities in the plasma with frequencies ranging from 50 to 500kHz were detected. The largest amplitudes of these fluctuations were located near the edge of the plasma spot. It is possible that keeper erosion may be mitigated by damping the RF fluctuations in the plasma.

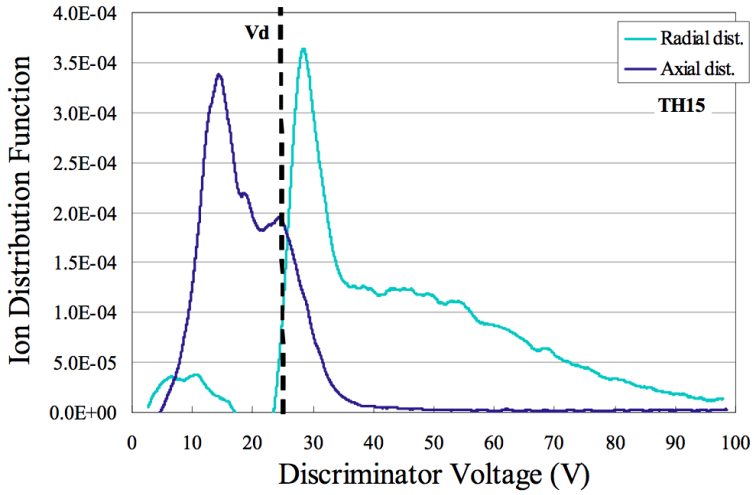

Figure 7: Ion Energy Distribution With Discharge Voltage Indicated for Reference[4]

Emissive probe measurements showed a dip in the radial plasma potential distribution near the centerline. It has been hypothesized that this dip in potential is the cause of the high-energy ions traveling radially.[4] Ions are accelerated toward the centerline, where there is a higher concentration of neutral particles. As the ions interact with the neutrals, some of them are neutralized by resonant charge exchange collisions, while maintaining their high velocity. The high-speed neutral particles pass through the center of the potential dip, and are again ionized then further accelerated by the potential gradient away from the centerline. This process is called a double charge exchange collision.The result would be a small population of high-energy ions. Figure 8 (adapted from Katz[4]) is a diagram of the proposed double charge exchange mechanism. The radial variation in plasma potential has a dip in the center, near the orifice, and this dip may be responsible for the production of high-energy ions.

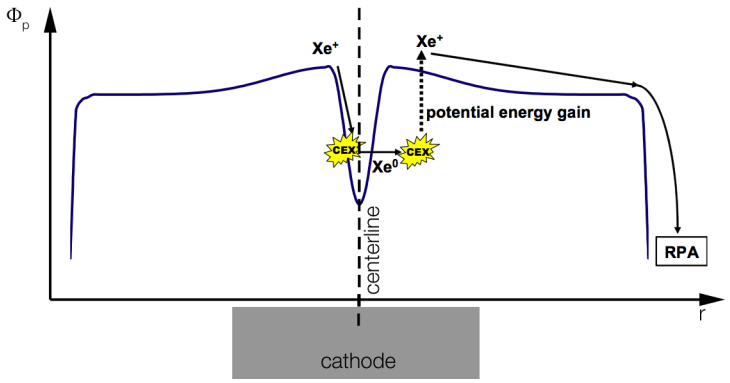

Figure 8: High-Energy Ion Production Via Potential Dip[4]

Using boundary conditions from experimental data, a two-dimensional model of the plume region plasma was generated based on a simplified version of Ohms Law.[4] The contour of the plasma potential was consistent with the radial distribution generated from the RPA measurements. The two peaks in the radial potential profile are a result of the increased ion density just off-axis. The trajectory of a particle was calculated based on the electric field, and used to determine the probability of a double charge exchange collision ocurring. A spectrum of ion energies was then generated based on the depth of the potential well. Figure 9 is a comparison of the calculated and experimentally determined distribution functions. The discharge voltage is again indicated by a vertical line. Katz points to sputtering by radially traveling ions as a possible mechanism for keeper erosion.

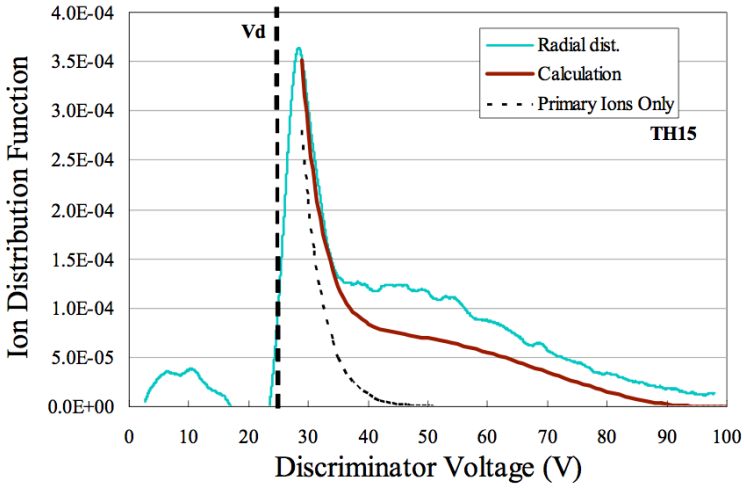

Figure 9: Comparison of Calculated Ion Distribution Function[4]

Mikellides *et al.*[13] developed a two-dimensional model of the the insert, orifice and plume regions of a hollow cathode. The objective was to predict electron temperature and number density variation in the plume and to test the viability of the double charge exchange theory. The 2-D Orificed Cathode code (OrCa-2D) assumes a continuum fluid in the insert and orifice regions, and a collisionless, non-continuum model in the plume. The model predicts a sudden drop in plasma density with increasing axial distance. This rapid change in density is an exaggeration of the what is observed in experimental data. The code was then modified to account for a larger electron-neutral collision cross section due to high speed drifting electrons. The EEDF is assumed to be Maxwellian at this stage. The study concludes that accounting for electron drift yielded an appreciable improvement in the number density prediction. The authors note that deviations from the Maxwellian EEDF are not accounted for, but this knowledge might be insightful in assessing the double charge exchange theory.

Herman and Gallimore[16] used Langmuir probe data to measure the electron energy distribution function (EEDF) of the plume near the DCA of NASAs Evolutionary Xenon Thruster (NEXT). A high-speed axially reciprocating probe (HARP) was used to quickly take readings with minimal disturbance. A single-peak distribution was measured near the orifice, but

then gave way to a double-peak structure further downstream in the double layer. The second peak in the energy distribution was attributed to radially accelerated particles traveling across the double layer. Two analysis methods were employed. In the Druyvesteyn Method, the EEDF is proportional to the second derivative of the I-V characteristic. Differentiating experimental data introduces a significant amount of error, so multiple data sets were averaged, and various smoothing algorithms were applied to eliminate noise. The second method used, called the Harmonic Method, involves superimposing an AC signal on the probe voltage. This gives rise to a perturbation in the DC current collected, which is proportional to the second derivative. The advantage of this method is that the second derivative can be measure more directly, without having to numerically differentiate the data. It is clear that the EEDF is not necessarily Maxwellian everywhere in the plume. Most probe theories that are used to determine parameters such as plasma potential assume that the EEDF is Maxwellian.

Godyak[17] discusses the application of both the Druyvesteyn and Harmonic methods for measuring the EEDF. The two main assumptions in the analysis are (1) the velocity distribution is isotropic and (2) the plasma is collisionless at the relevent length scale. That is the probe diameter, probe holder diameter, and Debye length must be less than the electron mean free path.

$$d_p, d_{ph}, \lambda_D \ll \lambda_e \tag{7}$$

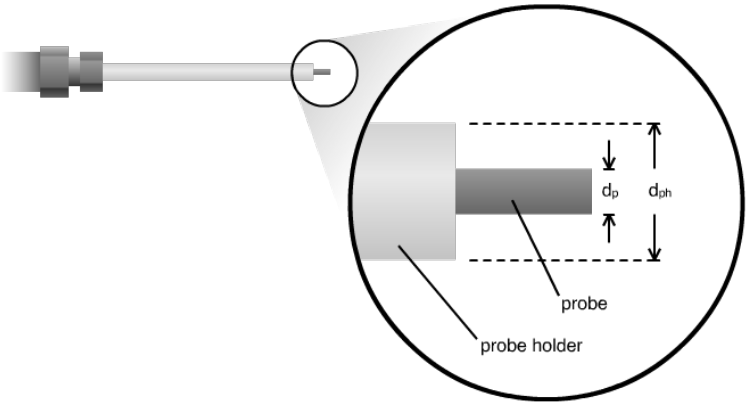

Figure 10: Probe and Probe Holder Diameter

The EEDF is related to the probe characteristic by the Druyvesteyn formula. The application of this formula is central to the Druyvesteyn Method for interpreting Langmuir probe data.

$$F(\epsilon) = \frac{4}{e^2 A_p}\left(\frac{mV}{2e}\right)^{\frac{1}{2}}\frac{d^2I}{dV^2}, \quad \text{where} \quad V = \phi_p - V_p \tag{8}$$

In the Harmonic Method, a constant DC voltage is applied to the probe, and an AC signal with amplitude $\partial(t)$ is superimposed over it. A Taylor Series expansion done about the DC voltage, V_o reveals an important relation for the second derivative.

$$I(V) = I(V_o + \partial(t)) = I(V_o) + \partial(t)\frac{dI(V_o)}{dV} + \frac{1}{2}(\partial(t))^2\frac{d^2I(V_o)}{dV^2} + ... \tag{9}$$

The oscillations in the measured probe current have frequency components due to the applied AC signal $\partial(t)$ and the second harmonic $(\partial(t))^2$ which is proportional to the second derivative of current with respect to voltage. Since the applied signal is known, it is subtracted from the data, leaving the second harmonic component, so that the Druyvesteyn formula can be applied. The higher order terms in equation (9) have negligible contributions provided that the magnitude of the AC signal is small compared to the mean electron energy.[18]

When applying the Druyvesteyn method, the probe is swept through a range of voltages, while the current is measured. Godyak[18] used a basic filter and differentiator circuit to process the probe current signal. This raised the question of the bandwidth for the differentiator circuit. If the bandwidth is too low, it can be a significant source of noise. A clear alternative would be to measure the raw I-V characteristic, then filter and differentiate numerically. Hopkins and Graham[19] applied such a technique successfully. Averaging multiple measurements smoothed the curve initially, and the first derivative was taken numerically. A polynomial fit was applied to the first derivative, and that polynomial was then differentiated.

Sawlani and Foster[20] provide a comprehensive summary of numerical methods for treating Langmuir probe data in order to extract the EEDF. In one of their studies, they took an ideal probe trace based on a Maxwellian EEDF with prescribed T_e and n_e, and superimposed simulated noise on the trace. Various smoothing methods are applied to the simulated data and the T_e and n_e are calculated using the Druyvesteyn formula. The error in the parameters is reported for each case.

The method of applying numerical techniques to the raw data has a distinct advantage over hadware-based methods in that the smoothed data can be compared to the original to determine what information is lost in the smoothing process. It is important that the smoothing technique preserve important features of the data set while eliminating noise.

In the Savitzky-Golay method, a polynomial is fit to a subset of data points. The center point of the fitted polynomial is used as the smoothed value at that location, and this process is carried out at each point. The effect is that the neighboring points are used in a weighted average, where the polynomial is the weighting function. The polynomial $p_i(x)$ is of order M and is fit using a least squares method.[20]

$$p_i(x) = \sum_{k=0}^{M} b_k \left(\frac{x - x_i}{\delta x} \right)^k \tag{10}$$

Sawlani and Foster[20] examined data sets of 150, 650, 1000, and 60000 points. They Savitzky-Golay method worked well in cases with fewer total data points. With 150 data points, they found an optimal window size of 27 points and an optimal polynomial order of 6.

Sawlani and Foster also applied a version Hayden Method in which the filtered data h_n is the convolution of the original signal h and a gaussian instrument function g_n. The instrument function is intended to be a hardware-specific function related to the error in the measurement of the probe current. Because of the difficulty in determining such information, a gaussian distribution is used.

$$h_n = h \otimes g_n \tag{11}$$

Swalani and Foster indicate having some success with the gaussian Hayden method, but do not offer a solid conclusion on it's effectiveness. Numerical artifacts were manifested in artificial oscillations in some cases.

Windowing methods use a periodic weighting function on a subset of points, much like the way the Savitzky-Golay method uses a polynomial weighting function. Sawlani and Foster use a cosine weighting function and found that windowing methods performed well for large data sets. Larger window lengths were optimal. These methods were also susceptible to artificial oscillations.

In the Sawlani and Foster[20] study, the use of polynomial fitting was found to be less effective in smoothing the data, and introduced artificial oscillations. This method was deemed inadequate for smoothing I-V traces.[20] The free four parameter fitting method fits a hyperbolic tangent function to the I-V curve.

$$I = exp\left[a_1 tanh\left(\frac{V_p + a_2}{a_3}\right)\right] + a_4 \tag{12}$$

This method was found to introduce significant variation depending on the coefficients chosen, and did not perform well in general.

1.4 Motivation and Overview of Experiment

Ion and Hall thrusters produce comparatively low thrust and must be operated for extended periods of time in order to deliver an appreciable impulse to the spacecraft. This places demanding lifetime requirements on the devices. One limiting factor in the lifetime of an ion thruster is the discharge cathode assembly. During operation, the hollow cathode keeper electrode may be eroded by high-energy ion bombardment. The exact cause of this population of high-energy ions is not completely understood. Retarding Potential Analyzers (RPA) and Langmuir Probes are the diagnostics most commonly used to characterize the plasma plume in the interest of developing a better understanding of the plume dynamics. RPAs are useful for determining ion properties, and measurements have detected high-energy ions, but not the source. Langmuir probes can be used to measure properties of the electron population in the plasma. The more common analyses of probe data rely on the assumption that the electron energy distribution function (EEDF) is Maxwellian. Experimental evidence suggests that in certain cases this assumption is not necessarily valid, particularly in low current cathodes.

Mikellides *et al.*[13] note that the frequency of electron collisions in the plume is low enough where the EEDF can deviate from the Maxwellian. This experiment focuses on an application where the EEDF is likely not Maxwellian, in order to determine how cathode operating conditions affect the energy distribution. The objective is to evaluate the properties of the plume, including the plasma potential, number density, electron temperature, and EEDF.

In this experiment, a Langmuir probe is used to determine the number density, electron temperature, plasma potential and electron energy distribution of the plume region plasma. A Langmuir probe is a bare wire that is inserted in the plasma to collect current. The applied voltage is varied while measuring the current to generate a plot of current versus voltage, or an I-V characteristic. The I-V characteristic is analyzed to determine the electron temperature T_e, plasma space potential ϕ, and plasma density n_e. A smaller diameter wire

will have better spatial resolution at the risk of being heated too quickly by the plasma. It is possible for the wire to be heated to the point where thermionic emission will affect the measurement and the behavior of the probe. A larger diameter wire will yield a cleaner signal at the expense of spatial resolution.

All measurements were taken at an axial distance of 1.0 cm from the keeper orifice with a constant flow rate of argon gas. The pressure of the chamber was constant at 2.9×10^{-5} Torr. Data was recorded for two sets of operating conditions. In each set, the anode power supply is operated in current-limited mode, and set to a specific value. A set consists of several passes. A pass refers to one traverse of the probe through the plasma. During a pass, the probe voltage is varied in a sawtooth pattern, and the current is measured. Several I-V curves are generated from each pass. Passes 1-17 are designated as Case 1, while passes 18-28 make up Case 2.

	Case 1	Case 2
I_{anode}	Baseline	133% Baseline

Table 2: Test Conditions

2 Probe Theory

2.1 Review of Kinetic Theory

The concept of the velocity distribution function is central in equilibrium kinetic theory. Particles in a gas will have different velocities, and each particles velocity will be changing due to interactions with other particles. A particle in a gas can theoretically have any velocity, however some velocities are more probable than others. A velocity distribution function relies on the assumption that at any time there is statistical probability that some number of particles will have a certain velocity. The concept of velocity space is introduced to better illustrate this idea. Cartesian velocity space coordinates are defined by C_1, C_2, C_3 as opposed to x, y, z in spatial coordinates. The velocity distribution in velocity coordinates is similar to mass distribution in spatial coordinates. Just as a differential element in configuration space will have a number of particles in a volume $dV = dxdydz$, a differential element in velocity space $dV_C = dC_1dC_2dC_3$, will have some number of particles in it. These particles will have a velocity in the x-direction between C_1 and $C_1 + dC_1$, a y-direction velocity between C_2 and $C_2 + dC_2$ and so forth. The distribution function $f(C_i)$ defines the fraction of the total number of particles that occupy the differential velocity element dV_C. If N is taken to be the total number of particles, then the number of particles in dV_C is

$$dN = Nf(C_i)dV_C \tag{13}$$

Since the distribution function gives the fraction of particles in a velocity element, the function integrated over all possible velocities must be equal to unity.

$$\int_{-\infty}^{\infty} f(C_i)dV_C = 1 \tag{14}$$

It is sometimes convenient to work with the non-normalized distribution function. This is simply a matter of multiplying by the number density.

$$F(C_i) = nf(C_i) \tag{15}$$

The distribution function $f(C_i)$ essentially provides the information on which velocities are more probable than others. Clearly, nearly infinite velocities are improbable, which gives some insight to what the function should look like.

Similar to the velocity distribution, the energy distribution function $F(\epsilon)$ defines the total number of particles that have an energy ϵ. If the energy distribution function is known, the number density and temperature can be calculated. The number density is equal to the integration of the distribution function over all energies, and the temperature is equal to two-thirds the average energy. This is true for any generalized distribution function $F(\epsilon)$.

$$n = \int_0^\infty F(\epsilon) d\epsilon \tag{16}$$

$$T = \frac{2}{3}\langle\epsilon\rangle = \int_0^\infty \epsilon F(\epsilon) d\epsilon \tag{17}$$

2.2 Distribution Functions

2.2.1 Maxwellian Distribution

The velocity distribution for a gas in equilibrium is given by the Maxwellian Distribution. The expression is the product of three distribution functions for the velocity in each of the three principle directions.[21] The distribution is uniform and isotropic in configuration space

and also isotropic in velocity space.

$$f(C_i) = \left(\frac{m}{2\pi kT}\right)^{\frac{3}{2}} \exp\left[-\frac{m}{2kT}\left(C_1^2 + C_2^2 + C_3^2\right)\right] \tag{18}$$

The expression in equation (18) is the normalized form of the Maxwellian velocity distribution, meaning that the integration of the function equals one. The energy distribution is related to the velocity by starting with the familiar relation for kinetic energy of a particle with mass m.

$$\epsilon = \frac{1}{2} m \left|\vec{v}\right|^2 \tag{19}$$

Since the energy is related to the magnitude of the velocity, it is useful to work in terms of the speed distribution function.

$$\chi(C) = 4\pi \left(\frac{m}{2\pi kT}\right)^{\frac{3}{2}} C^2 \exp\left(-\frac{m}{2kT} C^2\right) \tag{20}$$

Particles having a speed between C and $C + dC$ have energies between ϵ and $\epsilon + d\epsilon$.

$$f(\epsilon) d\epsilon = \chi(C) dC \tag{21}$$

The normalized energy distribution function is equal to the normalized speed distribution function multiplied by the derivative of the speed with respect to energy.

$$f(\epsilon) = \chi(C) \frac{dC}{d\epsilon}, \quad \text{where} \quad \frac{dC}{d\epsilon} = (2m\epsilon)^{-\frac{1}{2}} \tag{22}$$

It is now possible to write the normalized energy distribution function.

$$f(\epsilon) = \frac{2}{(kT)^{\frac{3}{2}}} \sqrt{\frac{\epsilon}{\pi}} \exp\left(\frac{-\epsilon}{kT}\right) \tag{23}$$

2.2.2 Druyvesteyn Distribution

The energy distribution of a gas is not always described by the Maxwellian. One example of a non-Maxwellian or non-equilibrium distribution is the Druyvesteyn distribution. The Druyvesteyn distribution was derived specifically for the EEDF in gas discharges in which the electron temperature is much greater than the ion and neutral temperature. This is the primary distinction between the Druyvesteyn and Maxwellian distributions.

The derivation to be presented is a summary of the one published by Druyvesteyn[22]. The Druyvesteyn EEDF is based on hard sphere collisions between electrons of energy ϵ and stationary ions or neutrals in an electric field E. The amount of kinetic energy lost in one collision is equal to twice the mass ratio times the original electron energy.

$$\Delta\epsilon = -\frac{2m_e\epsilon}{m_i} \tag{24}$$

The expression for energy loss in equation (24) is then expanded to represent the total energy loss for all electrons per unit volume, per unit time based on the mean free path λ and electron velocity v_e.

$$F(\epsilon)\frac{2m_e}{m_i}\epsilon\frac{v}{\lambda} = F(\epsilon)\frac{2m_e}{m_i}\frac{\epsilon}{\lambda}\sqrt{\frac{2\epsilon}{m_e}} \tag{25}$$

Druyvesteyn[22] equates equation(25) with the energy taken from the electric field.

$$J(\epsilon)eE = F(\epsilon)\frac{2m_e}{m_i}\frac{\epsilon}{\lambda}\sqrt{\frac{2\epsilon}{m_e}} \tag{26}$$

The electron current density $J(\epsilon)$ is the number of electrons passing through a unit area perpendicular to the electric field. The mobility equation is then used to write another equation for the electron current density.[22]

$$J(\epsilon,x) = -\frac{\lambda}{3}\sqrt{\frac{2\epsilon}{m_e}}\frac{\partial F(\epsilon)}{\partial x} - \frac{\lambda eE}{3}\sqrt{\frac{2\epsilon}{m_e}}\frac{\partial F(\epsilon)}{\partial\epsilon} + \frac{\lambda eE}{3m_e}\sqrt{\frac{m_e}{2\epsilon}}F(\epsilon) \tag{27}$$

Since the energy distribution is independent of the position x, the first term on the right hand side in equation (27) is zero. Substituting equation (26) into (27) yields a first order, one dimensional differential equation.

$$\frac{dF(\epsilon)}{d\epsilon} = F(\epsilon)\left(\frac{1}{2\epsilon} - \frac{6m_e\epsilon}{m_i\lambda^2 e^2 E^2}\right) \tag{28}$$

An expression for $F(\epsilon)$ is found from the solution to the differential equation in (28). The variable α is an undetermined coefficient.

$$F(\epsilon) = \alpha\sqrt{\epsilon}\exp\left[\frac{3m_e\epsilon^2}{m_i\lambda^2 e^2 E^2}\right] \tag{29}$$

Druyvesteyn[22] simplifies this equation, leaving it in terms of the average energy and eliminating the electric field term. The electric field dependence is only used for the derivation.

$$F(\epsilon) = \alpha\sqrt{\epsilon}\exp\left[-0.55\frac{\epsilon^2}{\langle\epsilon\rangle^2}\right] \tag{30}$$

Equation (30) can be rewritten in terms of the electron temperature by substituting equation (17).

$$F(\epsilon) = \alpha\sqrt{\epsilon}\exp\left[-0.243\left(\frac{\epsilon}{kT_e}\right)^2\right] \tag{31}$$

A specific expression for the Druyvesteyn electron energy distribution is given by Ming Li *et al.*[23]

$$f_D(\epsilon) = \frac{0.5648n_e}{(kT)^{\frac{3}{2}}}\sqrt{\epsilon}\exp\left[-0.243\left(\frac{\epsilon}{kT}\right)^2\right] \tag{32}$$

The most significant difference between the Maxwellian energy distribution in equation (23) and the Druyvesteyn distribution in equation (32) is the different power of ϵ in the exponential argument. Physically, the Druyvesteyn distribution is specific to electrons interacting

with neutrals of comparatively low energy. Figure 11 is a graphical comparison between the Maxwellian and Druyvesteyn distributions.

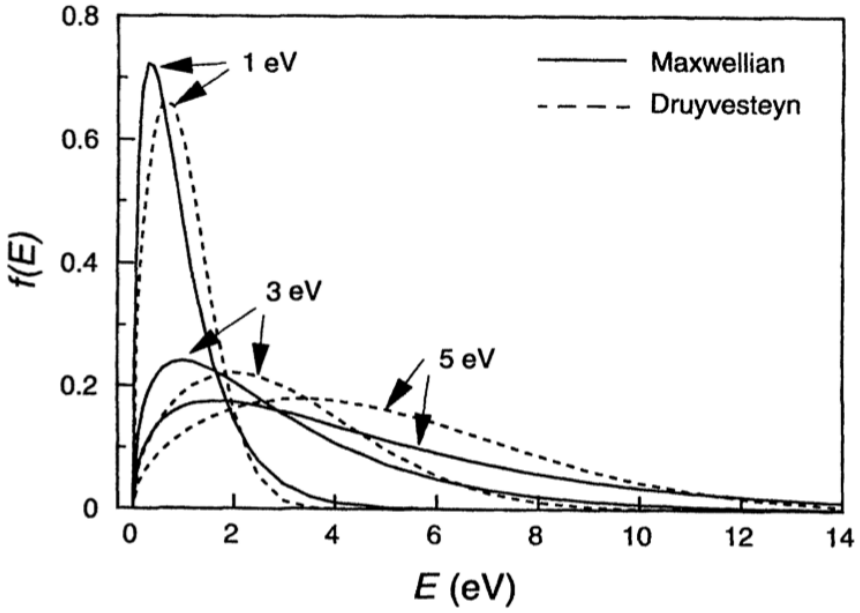

Figure 11: Comparison of Maxwellian and Druyvesteyn Distributions[5]

Electron-neutral collisions behave as hard-sphere collisions at low energies.[24] It is therefore possible that a Druyvesteyn distribution may be found in a low energy plasma.

2.3 Ideal Probe Current-Voltage Characteristics

Figure 12 shows an idealized I-V characteristic. The horizontal axis is the probe voltage, while the vertical axis is the current collected. Electron current is positive in the diagram. One an ideal characteristic, the point at which electron saturation is reached is called the knee of the curve and the probe voltage at that point is equal to the plasma potential. The probe voltage for which no net current is collected is the floating potential V_f. The potential within the sheath varies over the sheath thickness from the plasma potential at the sheath-plasma boundary to the probe potential at the probe surface. Ions and electrons with

enough kinetic energy are able to overcome the electric potential well and collide with the probe. When $V_p \gg \phi_p$, most ions are repelled and an electron current I_e is collected; when $V_p \ll \phi_p$, most electrons are repelled and an ion current I_i is collected. The sheath expands in the transition region between the V_f and ϕ_p, and both ions and electrons are collected.

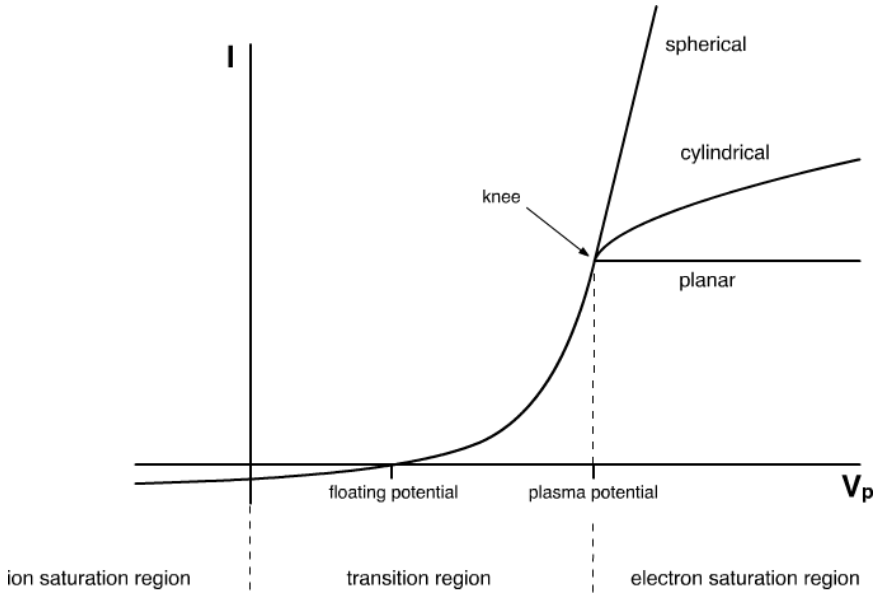

Figure 12: Ideal I-V characteristic

The shape of the curve is dependent on the probe geometry.[25] The characteristic from a planar probe has the most distinct knee and electron saturation. In the cases of a cylindrical and planar probes, the knee is at the inflection point of the curve. Electron saturation is the condition in which the maximum is reached for the flux of electrons to the probe. In the electron saturation region, the sheath continues to grow with increased probe voltage, while the flux remains constant. Electron current increases with increasing sheath surface area. Since the current varies in this region for spherical and cylindrical probes, the electron saturation current is a bit ambiguous at first glance. With a spherical probe, and no knee is observed. For a cylindrical probe, the knee is often rounded-off. When graphical interpretation of the probe characteristic cannot be carried out, the plasma potential may be obtained

from the maximum of the first derivative, or the zero of the second derivative of the curve with respect to probe voltage.

2.4 Probe Operating Regime

2.4.1 Sheath Size

Debye shielding is an important phenomenon to consider in designing a Langmuir probe experiment. A particle that strikes the probe directly will be collected, however not all particles that enter the sheath are necessarily collected. Since the potential within the sheath varies, the trajectory of a charged particle will be altered when it enters the sheath. Particles that were not on a collision course with the probe initially can be drawn into a trapped orbital path. If the sheath thickness is small compared to the radius of the probe, most of the current collected will be a result of particles colliding with the probe itself. This is referred to as the thin sheath case. As the sheath thickness increases, a larger fraction of particles are collected by the potential well surrounding the probe. The sheath thickness, δ is often only a few times the Debye length.[25] It can be calculated for cylindrical probes as a function of the Debye length and species masses.[26]

$$\delta = 1.02\lambda_D \left[\sqrt{-\frac{1}{2}\ln\left(\frac{m_e}{m_i}\right)} - \frac{1}{\sqrt{2}}\right]^{\frac{1}{2}} \left[\sqrt{-\frac{1}{2}\ln\left(\frac{m_e}{m_i}\right)} + \sqrt{2}\right] \tag{33}$$

According to Hershowitz, the sheath thickness is approximated well by the Debye length. A strongly negative probe bias can affect the sheath thickness however, and he presents an estimate for the dependence of sheath thickness on probe bias (relative to plasma potential).

$$\delta = 1.1\lambda_D \left[\frac{e\left(\phi_p - V_p\right)}{T_e}\right]^{\frac{3}{4}} \tag{34}$$

For cylindrical Langmuir probes where the Debye length exceeds the probe radius, $r_p/\lambda_D < 1$, the Orbital Motion Limit (OML) collection theory is appropriate.[27] In order to apply the thin sheath assumption, the probe radius must be much larger than the Debye length, $r_p/\lambda_D \gg 1$. Chen[28] specifies the criteria $r_p/\lambda_D > 10$ for thin sheath and $r_p/\lambda_D < 3$ for Orbit Motion Limited. Demidov *et al.*[29] provide a comprehensive breakdown for the validity of the Druyvesteyn method (defined in Section 2.7) in various regimes. The Druyvesteyn method can be applied in collisionless plasmas regardless of sheath thickness, as well as in a number of situations in collisional plasmas.

2.4.2 Collisionality

The bulk behavior of a gas is dependent on the characteristics of the collisions happening at the microscopic level. The Knudsen number is a dimensionless parameter that is used to categorize different flow regimes.[21] It will be important to know what regime best describes the plume region plasma, as the validity of any probe theory will be depend on this heavily. Table 3 gives approximate values for the boundaries between flow regimes.

$K_n > 10$	Free-molecular flow
$10 > K_n > .01$	Transitional
$1 > K_n > .01$	Slip
$K_n \ll .01$	Continuum

Table 3: Knudsen Numbers for Various Flow Regimes

The Knudsen number is defined as the ratio of the mean free path to a characteristic length of the domain. In Langmuir probe diagnostics, this characteristic length is typically

chosen to be the diameter of the probe.

$$K_n = \frac{\lambda}{L} \tag{35}$$

The mean free path for particles in a gas can be estimated based on the density of the gas and the size of the particles. If the particles are assumed to be identical with a diameter d, and have a mean speed $\bar{C}$, the mean free path is simply dependent on the rate at which a particle sweeps out volume.

The rate at which the molecule Z sweeps out volume is $\pi d^2 \bar{C}$. The number density gives the number of molecules per unit volume, so the number of molecules whose centers lie in the volume of the path of molecule Z is $\pi d^2 \bar{C} n$.[21] This quantity also represents the number of collisions per unit time for molecule Z. The mean free path can then be written as

$$\lambda = \frac{1}{n\pi d^2} \tag{36}$$

This simplified approach demonstrates that the mean free path is dependent on the size of the particle's sphere of influence, or cross section. In the case of an interaction between two neutral particles, the cross section is represented by the physical cross sectional area of the particle. For interactions between charged particles, the determination of the cross section is more involved.

The transfer of momentum is the basic event that drives diffusion and mobility in a gas.[6] The momentum cross section, σ_m, describes the rate of momentum transfer. The calculation of the momentum cross section for charged particle interaction begins with a potential function, $\phi(r)$ for a coulomb interaction.

$$\phi(r) = \frac{1}{4\pi\epsilon_o}\frac{qq_1}{r} \tag{37}$$

The incident particle m_1 approaches the target particle m with relative velocity g and impact parameter b, and is scattered through an angle χ. The distance of closest approach, r_m is given by

$$r_m = \frac{b^2}{-b_o + \sqrt{b_o^2 + b^2}}, \quad \text{where} \quad b_o = \frac{qq_1}{4\pi\epsilon_o \mu g^2} \tag{38}$$

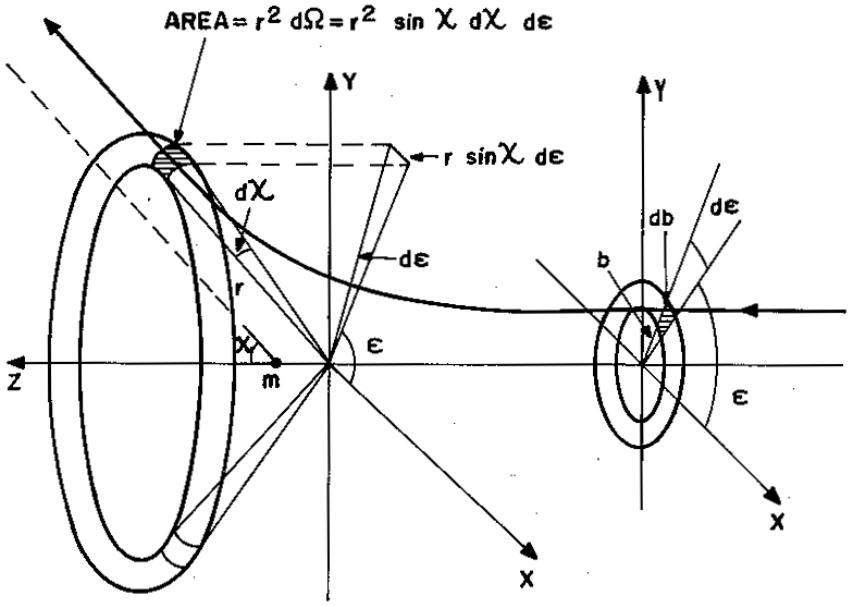

Figure 13: Differential Angles[6]

Figure 13 shows a coordinate system for a particle interaction. Particles passing through the differential area $bdbd\epsilon$ are scattered through the area $r^2 d\Omega$. The momentum cross section is defined by equation (39).

$$\sigma_m = 2\pi b_o^2 \int_{\chi_{min}}^{\pi} \frac{\sin\chi}{1-\cos\chi} d\chi \tag{39}$$

Since the Coulomb force is infinite, there is no mininum for the scattering angle, χ_{min}. To address this, a cutoff value χ_{min} is imposed which corresponds to an impact parameter

equal to the Debye length. This is an approximation for the effect of Debye screening as described in many elementary plasma physics texts, for example Bittencourt.[6]

$$\sigma_m = 2\pi b_o^2 \ln\left(1 + \left(\frac{\lambda_D}{b_o}\right)^2\right) \tag{40}$$

Equation (40) can be very well approximated assuming the Debye length is much larger than b_o, the impact parameter corresponding to a scattering angle of $\frac{\pi}{2}$.

$$\sigma_m = 4\pi b_o^2 \ln\left(\frac{\lambda_D}{b_o}\right) \quad \text{when } \lambda_D \gg b_o \tag{41}$$

The quantity b_o is dependent on the relative velocity g^2. In order to apply this method to calculate the mean free path of a gas, an average quantity must be used for g^2. Assuming a Maxwellian energy distribution, the average velocity is proportional to the temperature.[6]

$$\left\langle g^2 \right\rangle = \frac{3kT}{\mu} \tag{42}$$

The mean free path can then be calculated based on the momentum cross section.

$$\lambda = \frac{1}{\sigma_m n} \tag{43}$$

The potential $\phi(r)$ varies for different interactions. Therefore, mean free paths must be calculated differently for electron-ion, ion-ion interations, and so forth. For collisions with no coulomb interaction, the mean free path can be calculated using the simplified hard sphere model in equation (36).

Langmuir probes in a simulated space environment such as the facility used in this experiment typically operate in the collisionless regime. That is, the dimensions of the probe are smaller than the mean free paths of the plasma species. Since the plasma consists of ions,

electrons and neutrals, different mean free paths can be calculated for collisions between different combinations of particles. The collisionless condition must be verified in order to properly apply the collection theory.

For electron-ion collisions the mean free path is calculated using equation (43) and the cross section σ_m is determined from equation (41). For these collisions, the charges of an electron and a singly charged ion are used. The square of the relative velocity is replaced with the mean value for a Maxwellian distribution.

$$\lambda_{ei} = \left[4\pi n b_o^2 \ln\left(\frac{\lambda_D}{b_o}\right)\right]^{-1}, \quad \text{where} \quad b_o = \frac{-e^2}{12\pi\epsilon_o kT} \tag{44}$$

The procedure for determining the mean free paths for electron-electron and ion-ion collisions are analogous to the electron-ion case. The reduced mass μ, relative velocity $\langle g^2 \rangle$ and the charge of the particles will generate a different result. Collisions involving neutral particles can be calculated using equation (36) since there is no charge interaction. Experimentally determined cross sections are often used to examine collisionality. The rate at which collisions occur, or the collision frequency, for a Maxwellian plasma can be determined if the cross section is known.

$$\nu = \frac{n\sigma v_{th}}{\sqrt{2}}, \quad \text{where} \quad v_{th} = \sqrt{\frac{3kT}{m}} \tag{45}$$

Cross sections are tabulated for multiple different interactions including charge exchange and ionization collisions. This allows one to determine the frequency of such interactions.

The mean free path for electron-ion interactions will be the shortest by virtue of the attraction force. Consequently, this value is the critical parameter for the collisionless condition. In order for the collection of current to be considered collisionless, the mean free path for electron-ion collisions must be much larger than the probe diameter ($\lambda_{ei} \ll d_p$).[29]

Data from previous work was required to estimate the electron temperature and number density, and to predict what regime the probe used in the experiment might operate in. Goebel *et al.*[9] provides detailed data on the conditions at various distances from the keeper orifice for a cathode operating at 25A discharge current. Table 4 summarizes the data.

Flow rate(sccm)	Distance (cm)	n_e (m^{-3})	λ_D	r_p/λ_D	d_p/λ_{ei}	d_p/λ_{en}
5	1	1.8×10^{20}	7.8×10^{-7}	65	0.108	2.8×10^{-4}
10	1	1.4×10^{20}	8.9×10^{-7}	57	0.084	2.2×10^{-4}
5	2	4.0×10^{19}	1.6×10^{-6}	30	0.026	6.4×10^{-5}
10	2	2.0×10^{19}	2.0×10^{-6}	22	0.014	3.2×10^{-5}

Table 4: Range of operating conditions ($T_e = 2$eV)[9]

It was assumed the thin sheath analysis would be valid, based on these conditions as a first approximation. The cases where the distance to the orifice is one centimeter are arguably on the borderline in terms of collisionality. Since the discharge current of the cathode used in Goebel's work is much higher than that of the cathode used in this experiment, the number densities and electron temperatures he reports are expected to be an upper bound estimate. This could affect the validity of the thin sheath theory, so the assumptions on the operation regime were reevaluated once the results were obtained.

2.5 Thin Sheath Collection Theory

The thin sheath analysis assumes a collisionless plasma, Maxwellian electrons, and a sheath size several times smaller than the radius of the probe. The theory is applied the transition region of the I-V curve. In deriving the theory, the velocity distribution is assumed to be Maxwellian. The derivation to be presented is a summary of the one published by Lipschultz.[30] First, the Boltzmann relation applied. Number density falls off exponentially

from the number density at the boundary of the sheath.[31] The plasma potential ϕ_p, probe potential V_p and local potential $\phi(r)$ are all with respect to ground.

$$n(r) = n_\infty \exp\left(e\frac{\phi(r) - \phi_p}{kT}\right) \tag{46}$$

The current collected is dependent on particle flux to the probe. Total probe current is written as the net amount of charged particles reaching the probe multiplied by the elementary charge.

$$I = eA_p\left(\Gamma_i - \Gamma_e\right) \tag{47}$$

The ion flux to the probe is constant and can be written in terms of the velocity and number density at the sheath boundary.

$$\Gamma = n_i v_i \tag{48}$$

The speed of ions entering the sheath is equal to the Bohm velocity.

$$C_i = \sqrt{\frac{kT_e}{m_i}} \tag{49}$$

Assuming once again that the electrons are Maxwellian, the flux is written as a simple function of the average thermal speed.

$$\Gamma_e = \frac{1}{4} n_e \bar{C}_e \tag{50}$$

The average speed of Maxwellian particles is expressed in terms of the temperature.

$$\bar{C}_e = \sqrt{\frac{8kT_e}{\pi m_e}} \tag{51}$$

The expression for the ion speed in equation (49) is multiplied by the number density as described by equation (46) to express the ion flux at the sheath boundary. The term ϕ_s

represents the local potential at the sheath boundary with respect to ground. The electron flux is obtained from equation (50), again substituting (46) for the number density. The fluxes are substituted into equation (47) and the number densities at the sheath boundary n_e and n_i are replaced with the plasma density n by the quasineutrality assumption.

$$I = e\left[-\frac{1}{4}\bar{C}_e n A_p \exp\left(\frac{e(V_p - \phi_p)}{kT_e}\right) + \bar{C}_i n A_s \exp\left(\frac{e(\phi_s - \phi_p)}{kT_e}\right)\right] \tag{52}$$

The potential at the sheath boundary ϕ_s with respect to the plasma potential is obtained by solving Poisson's equation for the potential everywhere in the sheath.[30] The sheath potential is assumed to vary from the probe potential at the probe surface to the plasma potential at infinity. For the purpose of expressing the sheath boundary potential, the plasma potential is assumed to be much greater than the probe potential, and the resulting solution for the potential at the sheath boundary is independent of the probe potential. It will be shown later that the sheath boundary potential is used in the expression for the ion saturation current. This supports the assumption that the plasma potential is much greater than the probe potential, since ion saturation takes place at low probe voltages.

$$\phi_s - \phi_p = \frac{-kT_e}{2e} \tag{53}$$

The area of the sheath is approximately equal to the area of the probe, so only the probe area term A_p is used. The total probe current reduces to equation (54) by substituting equation (53) for the potential at the sheath.

$$I = eA_p\left[-\frac{1}{4}\bar{C}_e n \exp\left(\frac{e(V_p - \phi_p)}{kT_e}\right) + \bar{C}_i n \exp\left(-\frac{1}{2}\right)\right] \tag{54}$$

It is convenient to put this expression in terms of the ion and electron saturation currents.

$$I = I_{se} \exp\left(\frac{e(V_p - \phi_p)}{kT_e}\right) + I_{si} \tag{55}$$

The exponential relation between the electron current and probe bias is now more apparent. The electron and ion saturation currents are constants.

$$I_{se} = -\frac{1}{4} en\bar{C}_e A_p \tag{56}$$

$$I_{si} = enC_i A_p \exp\left(-\frac{1}{2}\right) \tag{57}$$

The transition region on the I-V characteristic between the floating and plasma potential is approximated as an exponential function and, in the ideal case, the probe current will appear as a straight line on a logarithmic plot. The electron temperature T_e can be determined from the slope of this line. The point at which an extrapolation of this line reaches the plasma potential corresponds to the electron saturation current in the case of a planar probe. Using this value, the plasma density is obtained from equation (56).

2.6 Orbital Motion Limit Collection Theory

In cases where the sheath thickness is comparable to the probe radius, particles that pass through the sheath can be drawn in to the probe. The Orbital Motion Limit (OML) theory accounts for the orbital path of a charged particle in the sheath. The derivation to be presented is a summary of the one published by Allen[7]. Particles approach with velocity v and impact parameter h and pass with a distance of closest approach, p.

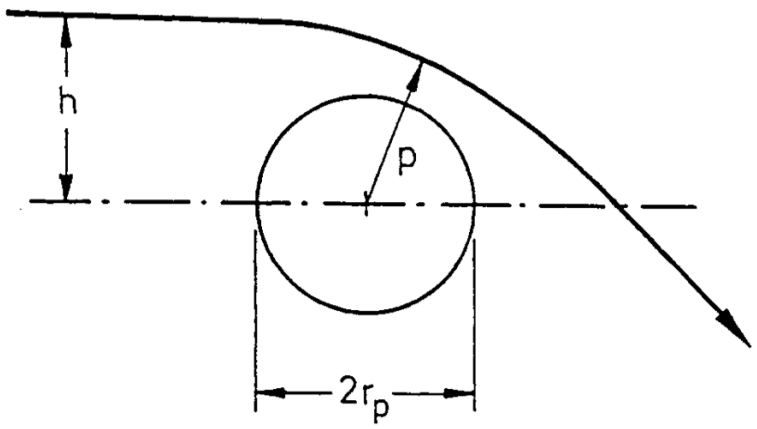

Figure 14: Trajectory of a particle passing through the sheath.[7]

Beginning with conservation of energy, the initial kinetic energy is equated to the sum of the kinetic and potential energy at closest approach.

$$\frac{1}{2}mv^2 = \frac{1}{2}mv_p^2 - eV_p \tag{58}$$

By conservation of angular momentum, the initial angular momentum equals the angular momentum at closest approach.

$$mvh = mr_p v_p \tag{59}$$

The critical impact parameter h_p corresponds to a grazing collision with the probe. The initial energy is defined as eV_o. A particle with energy eV_o will be collected if the impact parameter is less than the critical impact parameter.

$$h_p = r_p\sqrt{1 + \frac{V_p}{V_o}} \tag{60}$$

Electrons with energy eV_o within a distance of h_p from the probe are collected. If dn is the number of electrons with velocity v, then equation (61) gives the current contribution dI of

electrons with velocity v.

$$dI = 2\pi h_p l_p e \sqrt{1 + \frac{V_p}{V_o}} \frac{v}{\pi} dn \tag{61}$$

The number of particles occupying an element dv in velocity space for a Maxwellian velocity distribution is

$$dn = n \left(\frac{m}{2\pi kT} \right) \exp \frac{-mv^2}{2kT} 2\pi v dv \tag{62}$$

The differential current contribution of dn becomes

$$dI = \frac{2nr_p lme}{kT} v^2 \exp \frac{-mv^2}{2kT} \sqrt{1 + \frac{V_p}{V_o}} dv \tag{63}$$

The integration of equation (63) is integrated over all velocities yields the total current to the probe.

$$I = 2\pi n r_p l e \sqrt{\frac{kT}{2\pi m}} \left(\frac{2\sqrt{\eta}}{\sqrt{\pi}} + \exp(\eta) \operatorname{erfc}\left(\sqrt{\eta}\right) \right) \quad \text{where} \quad \eta = \frac{eV_p}{kT} \tag{64}$$

Allen[7] gives an approximation of equation (64) that eliminates the error function.

$$I = 2\pi n r_p l e \sqrt{\frac{kT}{2\pi m}} \frac{2}{\sqrt{\pi}} \sqrt{1 + \frac{eV_p}{kT}} \tag{65}$$

This approximation is very good for values of $\eta \geq 2$. The Probe voltage, V_p appears only once in the square root term. Therefore, the square of the I-V curve should be a straight line. The number density n is obtained from the slope of that line, and the electron temperature from the intercept.

2.7 Druyvesteyn Method for Electron Energy Distribution

According to Godyak,[18] the electron energy distribution function can be non-Maxwellian in some low pressure plasmas. In a non-Maxwellian distribution, there can be multiple peaks,

implying there exists more than one distinct population of electrons. As a result, defining the electron temperature as the mean energy in such a case would lead to erroneous results. The classical probe analyses such as the thin sheath and OML methods assume a Maxwellian energy distribution, and consequently yield an electron temperature that reflects the mean electron energy. The derivation of the Druyvesteyn equation to be presented is a summary of the one published by Lieberman and Lichtenberg.[24] The electron current is defined in general terms for an arbitrary EEDF. Electrons with a sufficient velocity component in the direction of the probe will be collected.

$$I_e = eA_p \int_{-\infty}^{\infty} dv_x \int_{-\infty}^{\infty} dv_y \int_{v_{min}}^{\infty} dv_z v_z f_e(v) \tag{66}$$

$$v_{min} = \left(\frac{2e\left(\phi_p - V_p\right)}{m_e} \right)^{\frac{1}{2}} \tag{67}$$

Equation (66) is rewritten in spherical coordinates and the distribution is assumed to be isotropic.

$$I_e = eA_p \int_{v_{min}}^{\infty} dv \int_0^{\theta_{min}} d\theta \int_0^{2\pi} d\phi v \cos\theta v^2 \sin\theta f_e(v), \text{ where } \theta_{min} = \cos^{-1} \frac{v_{min}}{v} \tag{68}$$

The dependence on ϕ and θ is eliminated by integrating over all angles.

$$I_e = \pi e A_p \int_{v_{min}}^{\infty} dv \left(1 - \frac{v_{min}^2}{v^2}\right) v^3 f_e(v) \tag{69}$$

This relation is put in terms of energy in electron volts by the substitution $\epsilon = \frac{1}{2} m v^2 / e$.

$$I_e = \frac{2\pi e^3}{m_e^2} A_p \int_V^{\infty} d\epsilon \cdot \epsilon \left[\left(1 - \frac{V}{\epsilon}\right) f_e\left(v(\epsilon)\right) \right] \tag{70}$$

Differentiating equation (70) twice with respect to V yields

$$\frac{d^2 I_e}{dV^2} = \frac{2\pi e^3}{m_e^2} A_p f_e\left(v(V)\right) \tag{71}$$

A relation between the energy distribution and the velocity distribution function is needed. The number of electrons with an energy within $d\epsilon$ is equal to the number of electrons having a corresponding velocity dv.[24]

$$F(\epsilon)d\epsilon = 4\pi v^2 f_e(v)dv \tag{72}$$

Equation (72) is rearranged as an explicit expression for the distribution function $F(\epsilon)$.

$$F(\epsilon) = 4\pi v^2 f_e(v)\frac{dv}{d\epsilon} \tag{73}$$

The velocity is related to the energy by the familiar equation in (74), and is differentiated with respect to ϵ.

$$v^2 = \frac{2\epsilon}{m} \tag{74}$$

$$\frac{dv}{d\epsilon} = \sqrt{\frac{1}{2m\epsilon}} \tag{75}$$

Equations (74) and (75) are substituted into (73).

$$F(\epsilon) = 4\pi\frac{2\epsilon}{m}\sqrt{\frac{1}{2m\epsilon}} f_e(v) \tag{76}$$

The velocity distribution function is proportional to the second derivative of the I-V characteristic as demonstrated in equation(71).

$$f_e(v) = \frac{m^2}{2\pi e^3 A_p}\frac{d^2 I}{dV^2} \tag{77}$$

Equation (76) is substituted into (72).

$$F(\epsilon) = \frac{4}{e^2 A_p}\sqrt{\frac{\epsilon m}{2e^2}}\frac{d^2 I}{dV^2} \tag{78}$$

This eliminates the velocity from the equation, and the energy ϵ can be removed by substituting $\epsilon = -eV$. The result is an expression for the EEDF that is dependent only on the second derivative of the probe characteristic.

$$F(\epsilon) = \frac{4}{e^2 A_p}\sqrt{\frac{mV}{2e}}\frac{d^2 I}{dV^2}, \quad \text{where} \;\; V = \phi_p - V_p \tag{79}$$

Equation (79) is referred to as the Druyvesteyn formula. Note the potential V is with respect to the plasma. The probe bias, V_p is measured with respect to facility ground, so the plasma potential ϕ_p is subtracted to give V with respect to the plasma.[18]. Once the EEDF is obtained, the number density and electron temperature follow according to basic kinetic theory.[32]

$$n_e = \int_0^\infty F(\epsilon) d\epsilon \tag{80}$$

$$T_e = \frac{2}{3}\langle\epsilon\rangle = \int_0^\infty \epsilon F(\epsilon) d\epsilon \tag{81}$$

The The thin sheath and OML theories assume a Maxwellian EEDF. If the EEDF is known, the temperature can be calculated by equation (81) thereby eliminating the need to make assumptions about the energy distribution. The EEDF can be determined using the Druyvesteyn method.

2.8 End Effects and Alignment Considerations

Non-spherical probes require attention to alignment and end effects. Since a sphere is radially symmetrical in all directions, while a cylindrical probe is symmetrical only in the r-θ plane. The asymmetry of a cylindrical probe gives rise to some often undesirable effects. The issues of alignment and the nature of the sheath at the tip can cause deviations from the orbit motion limited collection theory. Specifically, in a flowing plasma, a cylindrical probe oriented with the longitudinal axis aligned with the direction of flow can collect more ions than predicted by the theory.[8] Ions that would have ordinarily been repelled can have enough kinetic energy to pass through the sheath and strike the probe. Figure 15 shows the disparity

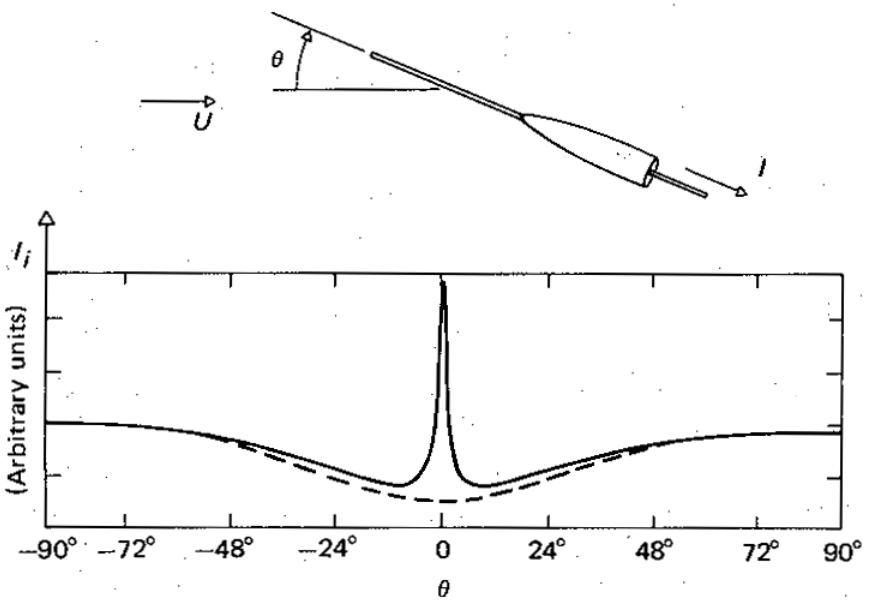

Figure 15: Deviation from OML theory for ion collection[8]

between predicted and measured ion current for small angle angles of attack. Angle of attack is the angle between the flow velocity vector and the longitudinal axis of the probe. The solid line in the figure represents the ion current from a cylindrical probe. The dotted line represents the current corrected for the end effect. When the probe is aligned with the direction of flow, ions enter the sheath at the end. In the derivation of the OML theory,

charged particles enter the sheath with an impact parameter and orbit in the direction of the curvature of the probe surface, transverse to the longitudinal axis. Orbital motions are not possible if a particle approaches a cylindrical probe at the tip in the direction of the longitudinal axis. For a cylindrical probe in a flowing plasma, the ideal alignment is at a 90 degree angle of attack. At zero angle of attack, ions approaching the tip of the probe do

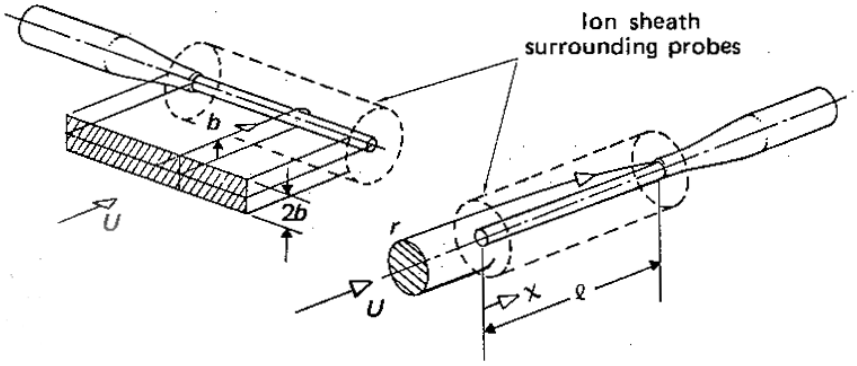

Figure 16: Illustration of the impact parameter for cylindrical probe[8]

not have an impact parameter as represented in the derivation of the orbit motion limited theory, and do not follow an orbital trajectory. This is referred to as the "end effect." The non-dimensional parameter τ_l is used to characterize the relative importance of the end effect.

$$\tau_l = \frac{l_p}{\lambda_D} \frac{\sqrt{kT_e/m_i}}{U} \tag{82}$$

Physically, τ_l represents the ratio of the probe length to sheath thickness multiplied by the ratio of the thermal velocity to the drift velocity. When $\tau_l \gg 1$, the end effect is considered negligible.[8] The end effect parameter is only a concern when the probe is directly aligned with the flowing plasma. This point is illustrated in Figure 15. In the collisionless regime, provided that the condition for the end effect parameter $\tau_l > 50$ is met, a cylindrical probe in a flowing plasma will behave the same as a probe in a stationary plasma.[8] If the end effect condition is satisfied, the drift velocity of the plasma can be ignored, and the analysis can

be carried out for a stationary plasma. This avoids the complexities of analyzing a plasma with a significant drift velocity. Alignment and end effects apply to ion collection, while this experiment focuses on electron collection. The effects are not important for electrons because of their lower mass and higher mobility. These effects are therefore not examined in the data analysis.

3 Experimental Setup

3.1 Facility

Experiments with the hollow cathode were conducted in the Vacuum Test Facility (VTF) in Higgins Labs room 016 on the main WPI campus. The VTF includes a 50in. $\times$ 72in. stainless steel vacuum chamber (Figure 17) and supporting instrumentation. The pumping system consists of a rotary mechanical pump, positive displacement blower combination with a pumping speed of over 560 liters/s (10^{-2} to 10^{-3} Torr). In addition, a 20in. CVI TM500 cryopump provides up to 10,000 liters/s on nitrogen, 8500 liters/s on argon, and 4600 liters/sec on xenon at pressures in the range of 10^{-4} to 10^{-7} Torr. The base pressure for this facility is in the mid-10^{-7} Torr range. Ancillary instrumentation includes a set of Pirani and hot cathode vacuum gauges and a mass flow meter. Pressure is measured using an MKS® Mini Ion Gauge hot cathode ionization sensor and Series 959 Hot Cathode Controller. Since all tests were conducted with Argon gas and the gauge is equally sensitive to argon as it is to air, there is no need to correct the pressure reading from the sensor.

Figure 17: Vacuum Test Facility in HL016

Figure 18 is a functional diagram of the gas delivery system. The gas supply is argon

regulated at approximately 25 psi. A Swagelok® SS-SVCR4 needle valve is used for precise control of the gas flow rate, and three Swagelok® SS-4-VCR4 diaphragm valves are used as shutoff valves. The MKS 179A Mass-flo® flowmeter is calibrated for Argon by measuring the analog output of the device for a known flow rate using a bubble volumeter. Connections on the gas feed system are made by welds and VCR fittings for leak integrity.

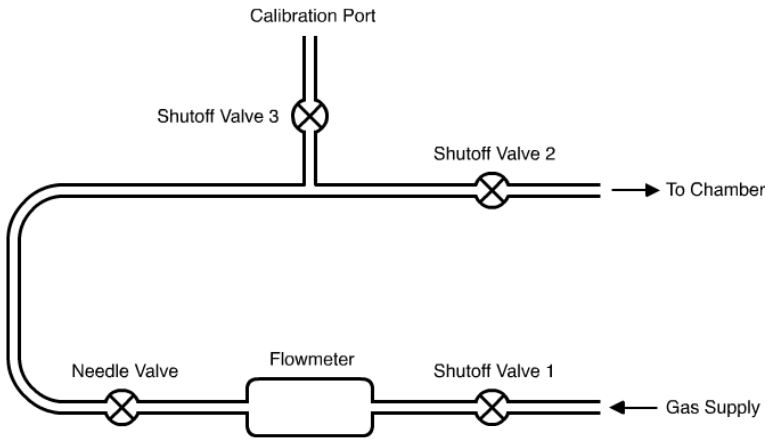

Figure 18: Gas Feed Control Panel

3.2 Cathode and Anode

The hollow cathode used in this experiment was a model BHC-1500 made by Busek Co. Inc. The BHC-1500 is used on Busek's 200 Watt hall thruster, the BHT-200, which was flown on TacSat 2, making it the first U.S. built and flight tested hall thruster.[33]

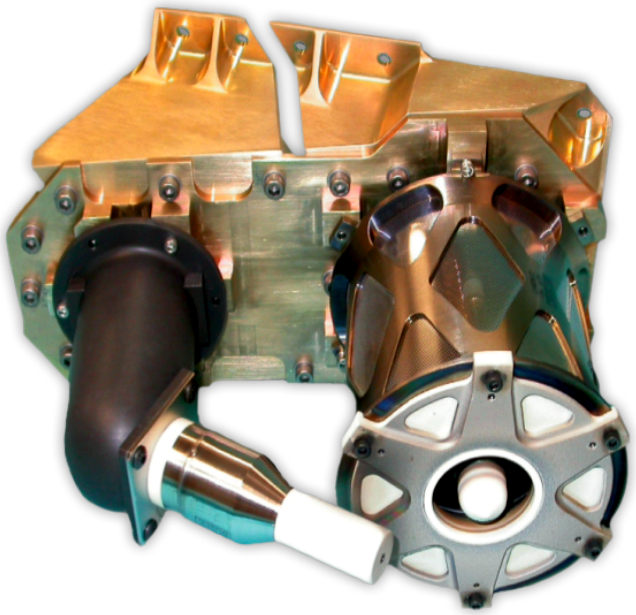

source: Busek Co. Inc. (www.busek.com)

Figure 19: Busek BHT-200 Hall Thruster with BHT-1500 Hollow Cathode

To start the cathode, current is applied to a resistive element in order to heat the insert to the point where it emits enough electrons to ionize the gas flowing through the cathode. The keeper electrode is biased positive by several hundred volts. If the gas has been sufficiently ionized, a conductive path is initiated between the cathode and the keeper. The high voltage applied to the keeper immediately collapses, and the keeper power supply switches to current-limited mode. When the discharge to the keeper is established, the cathode is said to be operating in diode mode. To simulate the plume from a hall thruster, a cylindrical aluminum tube surrounding the cathode is biased positive and serves as the anode. Two slots are milled out of the anode on either side of the cathode to accommodate the Langmuir probe (Figure 20). The anode geometry was based on a setup used by Fossum *et al.*[34] Figure 20 is a picture of the cathode and anode mounted in the vacuum chamber. When the cathode is discharging to the anode, it is said to be operating in triode mode. The insert region plasma heats the walls and orifice of the cathode and the heater can be turned off at this point.

Figure 20: BHT-1500 Hollow Cathode and Cylindrical Anode.

3.3 Probe and Positioning System

The Langmuir probe is made of a 0.076mm (0.004in.) diameter Tungsten wire, 2mm in length. The wire is supported and insulated by a 1.6mm (0.098in.) diameter single-bore alumina rod. The end of the alumina rod is sealed with Autocrete™ high temperature ceramic paste, providing additional support and isolation for the wire. The alumina is secured at the other end in a Swagelok® 0.0625in. × 0.25in. union. A short segment of stainless steel tube is slipped over the alumina, forming a sleeve to prevent the alumina from fracturing by relieving some of the compressive stress applied by the Swagelok® nut and ferrule. Figure 21 is a scaled drawing of the probe.

A low-magnification microscope is used to measure the length of the tungsten wire and verify that it is straight, and not bent to one side. Enamel magnet wire is sanded at either end to remove the insulation and fed into the alumina rod so it makes contact with the tungsten wire. The magnet wire is soldered to a segment of shielded cable, which is terminated with

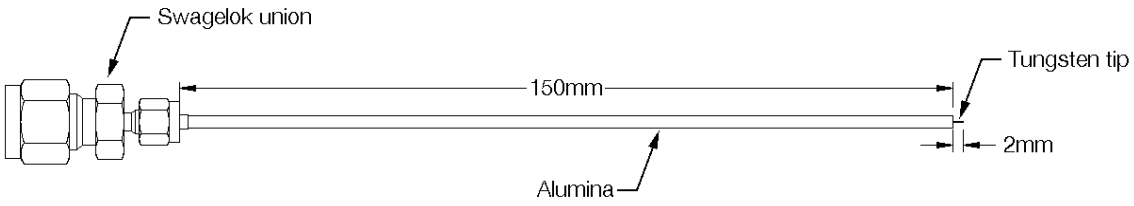

Figure 21: Diagram of Langmuir Probe

Figure 22: Photograph of Langmuir Probe

a BNC receptacle. The probe signal is carried to the chamber feedthrough by a BNC patch cable. The Swagelok® union at the base of the probe is supported by a 0.25in. stainless steel tube.

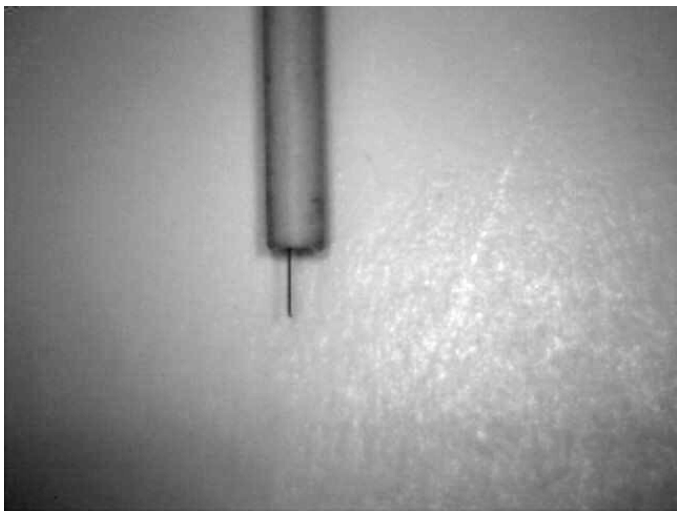

Figure 23: Probe Tip

Figure 24 depicts the geometry of the setup. The probe is oriented with the tip pointing back towards the cathode and mounted on a positioning system which allows motion only in the radial direction. All data presented is at an axial distance of 1cm from the keeper orifice.

In preliminary tests performed within 6mm of the keeper orifice, the probe was heated to the point where it began to glow orange. In order to avoid introducing additional error due to self emission, the probe was moved further away from the cathode. The probe positioning system consists of a linear actuator with a ball screw assembly. The ball screw is actuated by a Slo-Syn® stepper motor which is controlled by a Norberg BiStepA06 stepper motor controller. Motion commands are sent to the controller via serial port communication in LabVIEW.

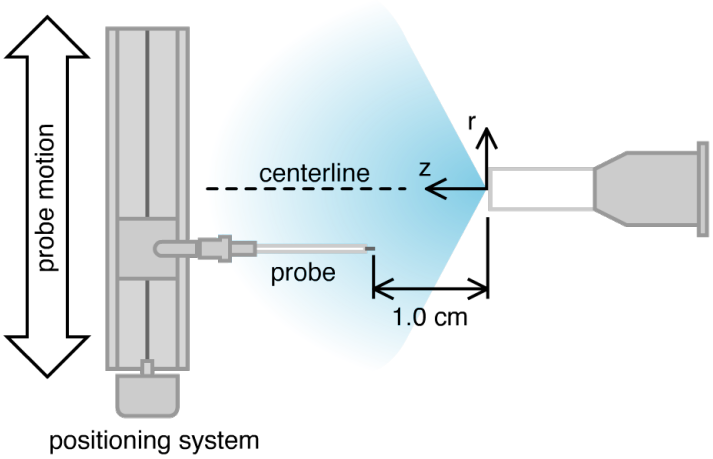

Figure 24: Top-Down View of Test Setup

Initially, attempts were made to measure the position using a linear potentiometer. One method involved applying 5 volts to the potentiometer and measuring the voltage drop between the 5V terminal and the wiper. Another method used an electrometer to measure the resistance between the wiper and one of the other terminals. In both cases, the resolution of the data acquisition system was insufficient to measure the position to within 1mm during bench tests. When the cathode was running, there was a significant amount of noise in the signal from the potentiometer, even when using shielded cable. This was presumably RF noise picked up the the potentiometer itself.

Next, a rotary encoder was employed. A US Digital® S4 Miniature Optical Shaft Encoder was attached to the threaded rod that drives the linear actuator. With this set up, the relative position was known to a high degree of accuracy. After several trials, the encoder system began to malfunction when tested with the cathode running. Eventually, the encoder stopped functioning entirely. This may have been avoided had the encoder been properly shielded.

The final solution to the position measurement employed a lever switch connected to a 5V power supply that would provide a pulse at two known locations. The switch is closed momentarily twice during each traverse across the orifice. When the switch is closed, the position of the probe is well-known. The probe begins moving and closes the switch. The position is then extrapolated based on the time and motor speed. The switch is closed again when the probe reaches the other side. The time between the pulses from the switch is used to confirm the probe speed by comparing the time with previous bench tests. It is assumed that the position varied linearly (i.e. constant speed). If the discrepancy was larger than 0.4 seconds, it is assumed that the positioning system malfunctioned, and the data for that test is not used. The main implication of using such a system is that there are no means of measuring the absolute position of the probe.

A minimal deviation in the time translates to an uncertainty in the position. The variability in the time for a single probe traverse was 0.39 seconds. At a speed of 1.186 mm per second, the variability in the probe position is .046mm. Therefore, the position of the probe is known to an accuracy of $\pm$0.23mm. This was acceptable for the purpose of this experiment.

As shown in Figure 24, when the probe is located off of the centerline, it is not aligned with the orifice. The angle of attack can be between 0 and 75 degrees depending on where the probe is located. The point at which the angle of attack is zero means the probe could be susceptible to end effects. The τ_l must be calculated from equation (82) to validate the

application of classical probe theory. Evaluation of τ_l requires an estimate for the ion drift velocity. The estimate is calculated assuming a neutral continuum fluid and that the flow in the orifice of the cathode is choked. For choked flow, the velocity in the orifice is equal to the speed of sound which can be evaluated based on the temperature of the gas.

$$a = \sqrt{\gamma RT} \tag{83}$$

Goebel[2] lists the ion temperature as ten percent of the electron temperature, and gives an electron temperature of 1.36eV in the insert region plasma for the NEXIS cathode. For a temperature of 1578K, the ion drift velocity is estimated at 400m/s. The end effect parameter is very large for this drift velocity. The conclusion is that end effects in this experiment are negligible for ion collection.

3.4 Data Acquisition System

The Data Acquisition system consists of a National Instruments® PCI-6024E Multifunction DAQ connected to an SCC-68 breakout board. The PCI-6024E is a 12-bit system with 16 analog inputs, maximum sampling frequency of 200 kHz, and a minimum voltage resolution of 0.106 mV. A Keithley 2410 Sourcemeter is used to supply the probe voltage and measure the current collected. The sourcemeter interfaces with the computer through a General Purpose Interface Bus (GPIB) card. A LabVIEW program exports code to the GPIB card, which the sourcemeter can then execute. The sourcemeter stores the data in its internal memory and transfers it to LabVIEW when the onboard buffer is filled. The data is stored as an ASCII file in the form of a single row matrix. A MATLAB code is used to import the data from the ASCII file and separate the single row matrix into current, voltage and timestamp readings. Since information from the sourcemeter cannot be passed to LabVIEW in real time, the timestamp is used to correlate the probe data with other data from the

test. Figure 25 is a diagram of the data acquisition setup.

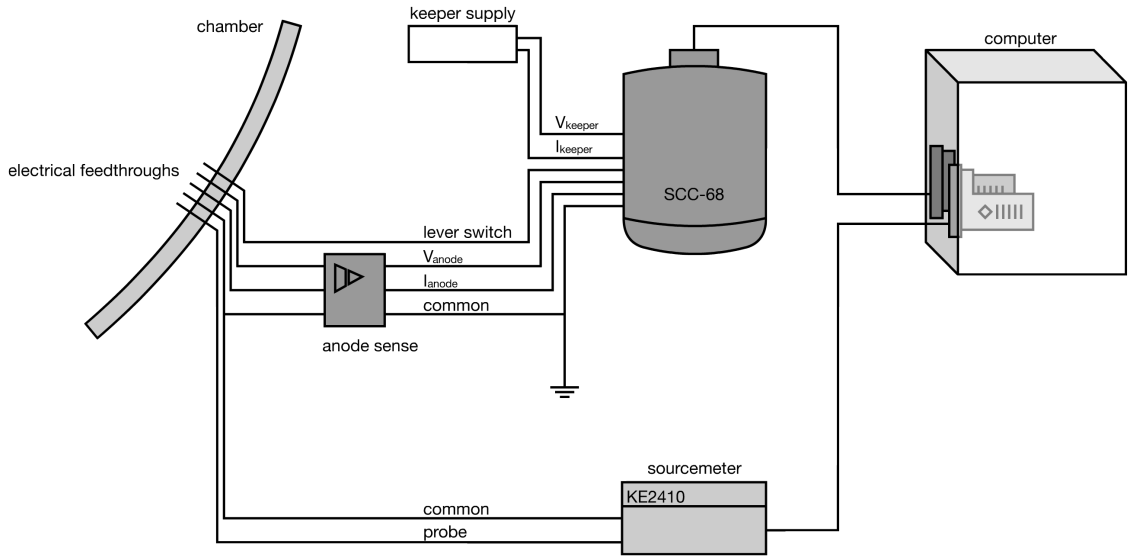

Figure 25: Diagram of Data Acquisition Setup

The sourcemeter has a current reading resolution of 1.2μA, and has a maximum voltage slew rate of 0.5V/μs. In practice, the maximum slew rate does not give a clear indication as to the time it takes to complete one sweep. The current measurement at a particular voltage takes an appreciable amount of time, and this amount of time varies. On average, a sweep containing 70 points lasts approximately one second. Although the term "sampling frequency" does not explicitly apply to this apparatus, it is a useful way to characterize the speed at which the data is taken. The sampling frequency is loosely defined as 70Hz, with the understanding that it is not particularly repeatable. Data is recorded as the probe travels at constant speed past the orifice of the cathode. Since the probe does not stop to take each measurement, a sweep takes place over a range of positions. The data set from one full sweep is used to calculate the plasma parameters, resulting in an uncertainty in the location for each measurement. For example, when the number density n_e is determined from a sweep that took place over a range of positions, there is an uncertainty in the location for that density. Narrowing the range of probe voltages for the sweep is a necessary step to

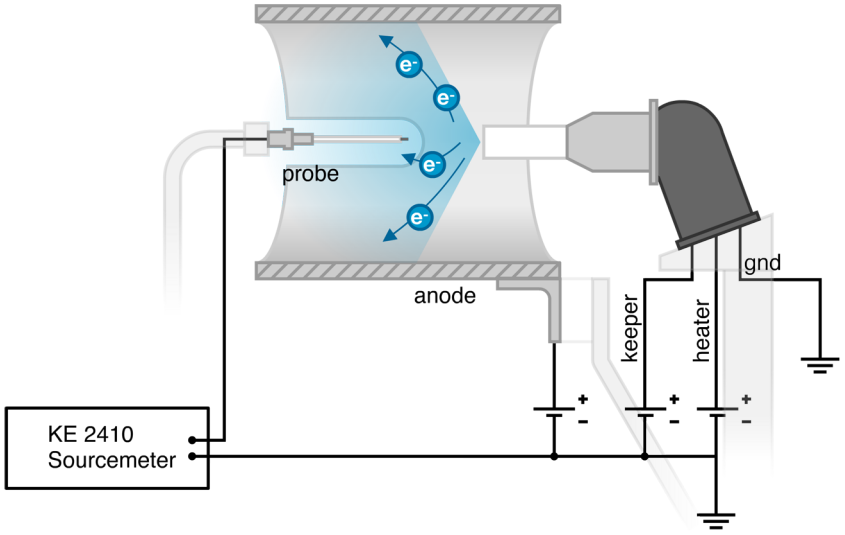

Figure 26: Diagram of Test Setup

maximize the fraction of relevant data points and keep the time down for a single sweep. This minimizes the uncertainty in the position for any parameter calculated based on the I-V curve. A sweep from -2 to 28V takes 1.746 seconds. During that time, the probe travels 2.08mm. The position for the I-V sweep is recorded at the half way point in the sweep, so the position uncertainty due to the voltage slew rate and probe speed is ±1.04mm. As stated earlier, the probe position is known to an accuracy of ±0.23mm. The overall uncertainty is the sum of the uncertainty due to the position measurement and the uncertainty due to the voltage sweep and probe motion. Table 5 summarizes the key parameters of the I-V sweep.

Voltage Range	Probe Speed	Voltage Step	Sweep Time	Position Uncertainty
-2 to 28 V	1.186 mm/s	0.25 V	1.746 s	±1.27 mm

Table 5: Probe Sweep Parameters

Conditions of the test such as chamber pressure, flow rate, keeper voltage and current and anode voltage and current are recorded by LabVIEW. Chamber pressure, flow rate, are read from analog outputs on the readout devices. Keeper voltage and current are read from

analog outputs on the keeper power supply. A voltage divider is used on the anode circuit to provide a proportional voltage that can be sensed by the DAQ. The anode current is calculated and recorded by measuring the voltage drop across a shunt resistor. An isolation amplifier with unity gain isolates the DAQ from the anode. The time is also recorded using the timer function in LabVIEW.

4 Determination of Plasma Parameters and Results

A sample of the raw data collected is shown in Figure 27. The most apparent feature of the curve is that it lacks a well-defined knee. The probe sweeps from -2 to 28 Volts. Tests with an expanded voltage domain show the same result. According to the thin sheath and OML theories, the I-V characteristic should have a clear saturation point at which the amount of current collected begins to diminish at higher probe voltages. Mostly ions are collected from -2V to the floating potential, which occurs at a probe voltage of 9V above ground.

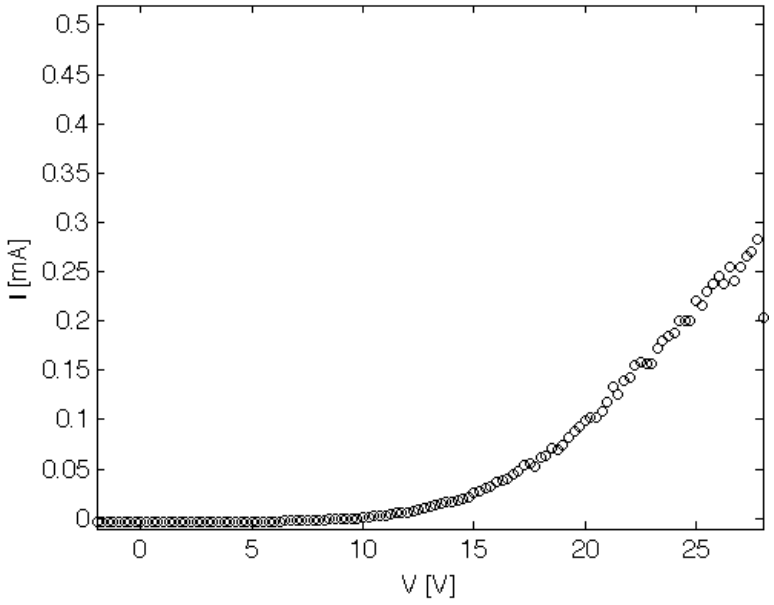

Figure 27: Sample I-V Characteristic

Determination of the plasma potential is especially difficult because there is no distinct knee in the raw I-V curve. Often a graphical method is sufficient to locate the knee and therefore the plasma potential, however this is not the case with the data obtained in this experiment. On an ideal I-V curve, the plasma potential also corresponds to the maximum of the derivative of the I-V curve, or the zero of the second derivative. It is necessary to examine the first and second derivatives to determine the plasma potential.

Differentiation of the probe data is done in steps. Since numerical differentiation of the

probe data amplifies the random noise in the curve considerably, a smoothing algorithm is necessary to obtain the first and second derivatives. The original I-V curve is smoothed, and the first derivative is obtained by a second order, central difference approximation.

$$\left.\frac{df}{dx}\right|_i = \frac{f_{i+1} - f_{i-1}}{2dx} \tag{84}$$

The same smoothing algorithm and difference approximation are applied to the first derivative to obtain the second derivative, to which the smoothing algorithm is also applied. Figure 29 shows the results for the first and second derivatives obtained by this process.

The Savitzky-Golay algorithm (described in section 1.3.2) is applied with various polynomial weighting functions. The most effective method used a polynomial order of one, or a simple weighted moving average. Higher order weighting functions are effective in removing random noise, but incur new oscillations. Sawlani and Foster[20] found an optimal polynomial order of six for their dataset. Their dataset had many more points, allowing them to use larger windows with higher order polynomials. The I-V curve in this experiment has fewer points, and cannot allow a window size large enough for higher order weighting functions to be effective.

In the ideal case, the plasma potential corresponds to the absolute maximum of the derivative, or the zero of the second derivative. Since this curve is not ideal, the first derivative does not have an absolute minimum and second derivatives do not have a zero. This is compounded by the fact that the curve must be smoothed in order to differentiate it. As an alternative, the first and second derivatives are examined for local maxima and minima, respectively.

A MATLAB® code was written to partially automate the calculation of the plasma potential. This is not a trivial task because, as seen in Figure (29), the plasma potential does not coincide with the absolute maximum of the first derivative or a zero in the second

derivative. The plasma potential is determined by three different methods and the three resulting values are averaged.

In the first method, a graphical technique is used. The data is plotted on a logarithmic scale to better visualize the departure from the exponential region. Two straight lines are fitted to the plot, and the intersection of the two lines indicates the plasma potential. An example is shown in Figure 28. Since the bend in the plot is still very slight, this method is insufficient on its own.

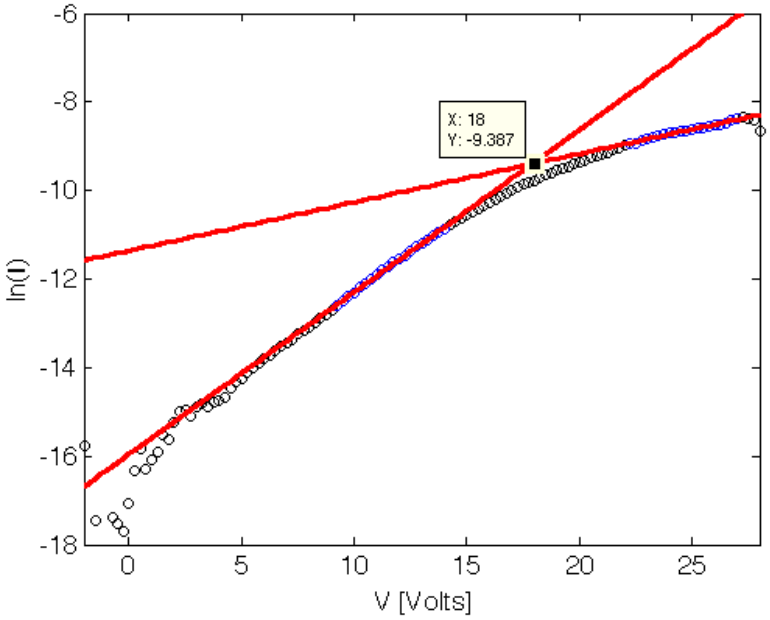

Figure 28: Curvefit For Determination of Plasma Potential

In the second method, the first derivative is examined. Since no absolute maximum for the first derivative exists within the domain, the local maxima are determined and examined as candidates for the plasma potential. First, a guess is made as to the expected value. This was determined by manually applying the curvefit method to several I-V curves. The curvefit method indicates that the plasma potential about 20 Volts for most tests. Therefore, the initial guess is 20 Volts, and the domain of interest is set to a range of 15 to 25 Volts. There are typically more than one local maxima near the guessed value. All of the local maxima

within a certain range of the guess are located, and the maxima that is closest to the initial guess value is used.

The second derivative is examined in the third method. Ideally, a maxima in the first derivative corresponds to a zero in the second derivative. However, since the second derivative is obtained by smoothing and then numerically differentiating the first derivative, it is possible that there will be no zero in the second derivative. The smoothing process often removes the local maxima in the first derivative. Even if the maxima is retained in the smoothing process, the numerical differentiation may not return a zero in the second derivative. Therefore, instead of attempting to locate a zero in the second derivative, the code searches for local minima in the second derivative. Similar to the second method that examines the first derivative, an initial guess of 20 Volts is used, and the local maxima closest to that point is identified as the location of the plasma potential.

Figure 29 shows the first and second derivatives. The plasma potential calculated by each of the three methods is marked with a dot on three of the plots.

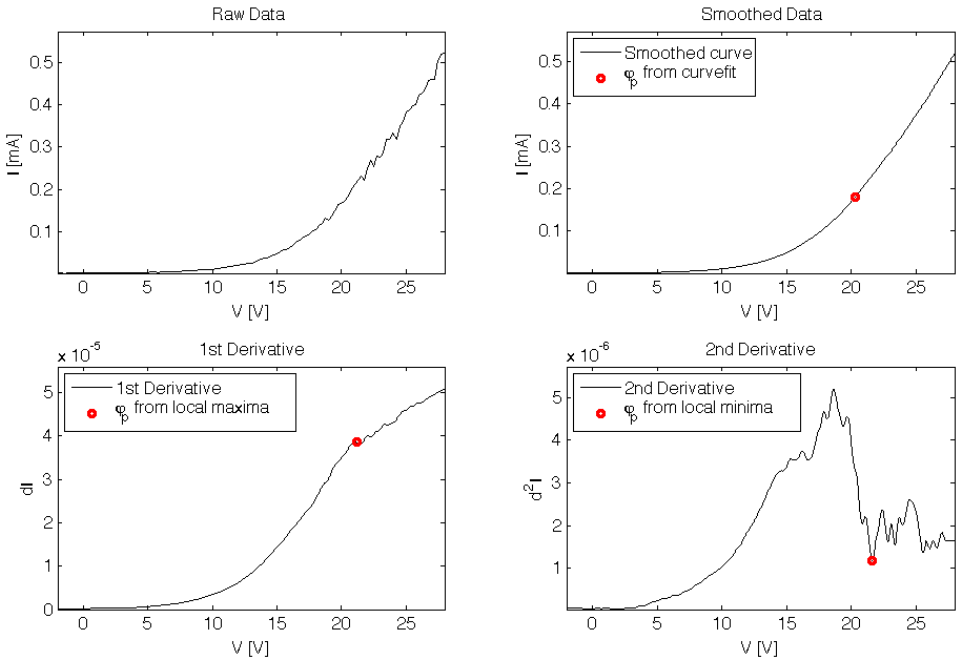

Figure 29: Smoothing and Differentiation of I-V Data

Figure 30 shows the different values for the plasma potential plotted together on a raw I-V curve.

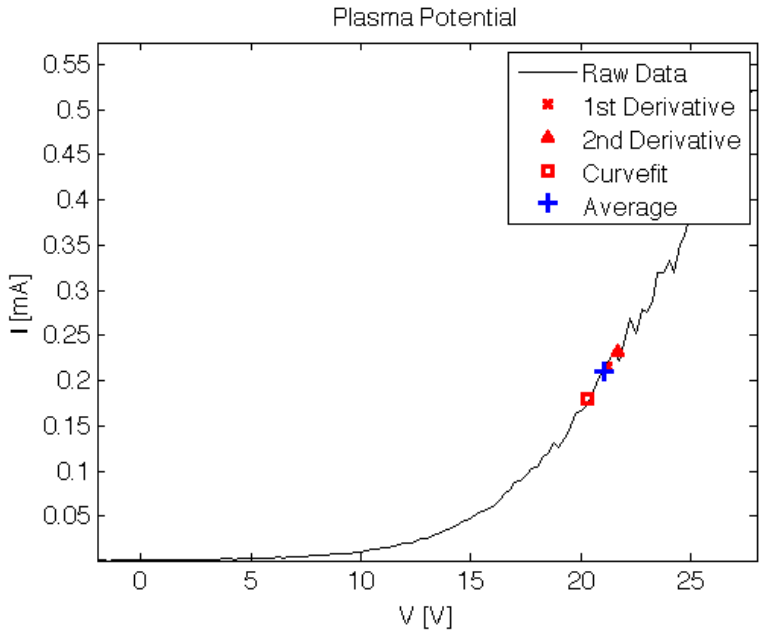

Figure 30: Plasma Potential Determination From Various Methods

	Curvefit	$\frac{dI}{dV}$	$\frac{d^2I}{dV^2}$	Mean
ϕ_p [V]	20.33	21.20	21.65	21.05

Table 6: Comparison of Plasma Potential Calculations

The three values for the plasma potential lie within a 1.3V spread, which is well within the 10V range that is examined by the code. Since the plasma potential calculation is carried out hundreds of times, it was important that it be automated. The drawback to automating this critical process is that the code sometimes identifies the plasma potential incorrectly. To mitigate this problem, the code performs all three methods for determining the plasma potential, and averages the values. The average of these three values is used as the final calculated plasma potential. In some cases there are no local maxima in the first derivative.

If the first derivative method fails for this reason, the plasma potential is an average of the two other methods. Using the average of the three methods produced plots of the potential with less scatter than plots generated using one specific method.

4.1 Implementation of Thin Sheath Probe Theory

The application of the thin sheath collection theory is based on an exponential dependence of electron current with probe voltage in the transition region. Ion saturation is approximated with a linear curvefit of the ion saturation region that is extrapolated over the entire domain of the data set. The ion saturation current is subtracted from the total current to give only the current due to electron collection.

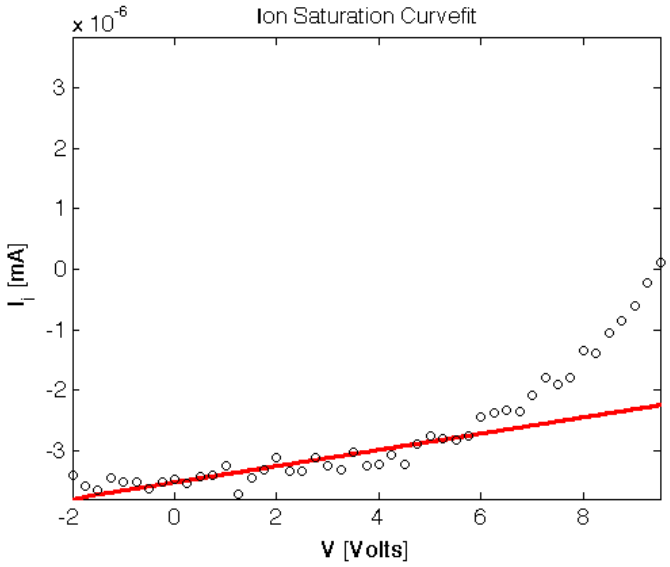

Figure 31: Linear Curvefit of Ion Saturation Current

The electron temperature is found by plotting the natural log of the electron current, and finding the slope of the line.

$$T_e[K] = \frac{e}{k}\left(\frac{d(\ln I_e)}{dV_p}\right)^{-1} \tag{85}$$

The electron saturation current is estimated by the current at which the curvefit crosses the plasma potential. This quantity is then used to determine the number density from equation (56) now that that electron temperature is also known. Figure 32 shows the exponential approximation of the electron current superimposed on the original data.

$$n_e = \frac{4I_{se}}{eA_p\bar{C}_e} \tag{86}$$

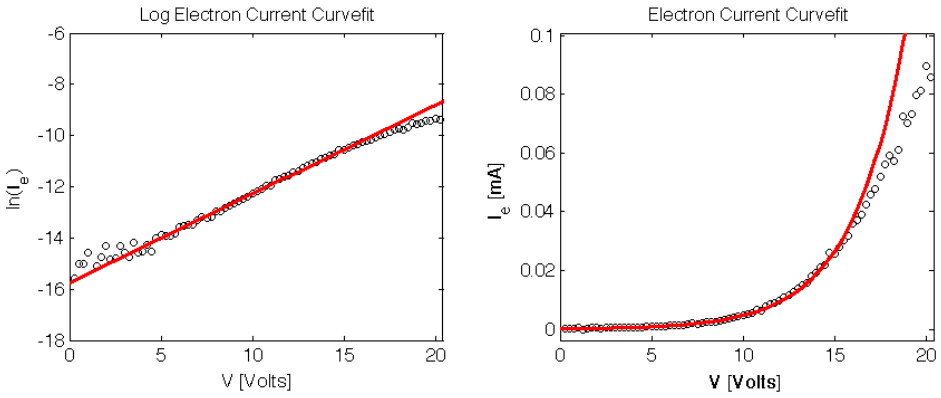

Figure 32: Exponential Curvefit of Transitional Region

This method is repeated for each I-V set as the probe passes the cathode. In Figures 33 and 34 the number density, electron temperature and plasma potential are plotted versus the position relative the centerline. For classical probe theories such as thin sheath and OML, Linell and Gallimore[26] estimate errors of 20% for number density and 50% for electron temperature. While these error values are significant, it is expected that error is relatively consistent across all measurements, and that the trends observed are representative of the true properties of the plume. As discussed in Section 3.4, the uncertainty in the position is ±1.27mm.

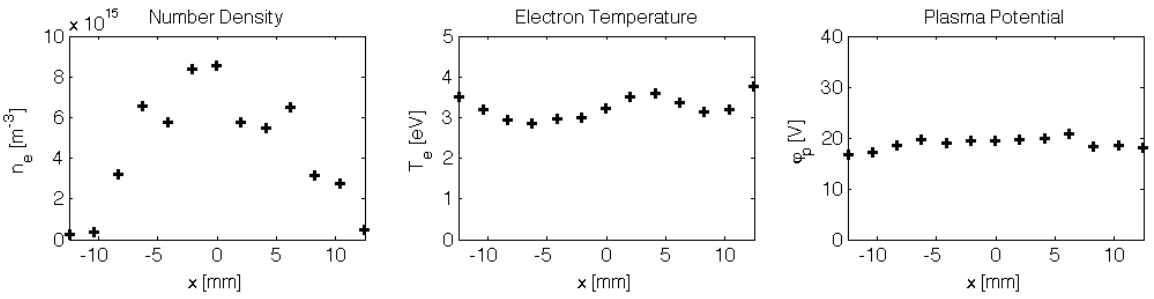

Figure 33: Radial Variation of Plasma Parameters for Case 1 - Thin Sheath

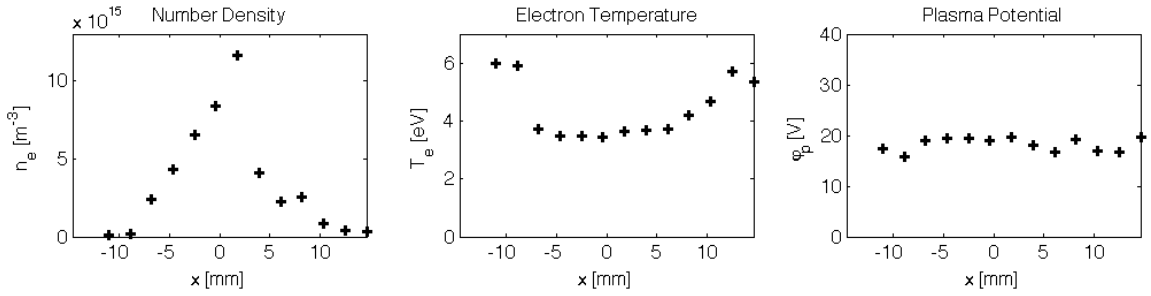

Figure 34: Radial Variation of Plasma Parameters for Case 2 - Thin Sheath

The assumptions for sheath thickness, Debye length and collisionality were reevaluated based on the plasma properties obtained from the theory. At these densities, the plasma is considered to be collisionless based on the criteria described earlier. As seen in Table 7, the mean free paths for electron-ion and electron-neutral interactions are many times larger than the probe dimensions.

	n_e (m^{-3})	T_e (eV)	λ_D (mm)	λ_D/r_p	δ (mm)	λ_{ei}/d_p	λ_{en}/d_p
Case 1	1.8×10^{16}	3.4	0.10	2.7	0.51	2.2×10^{5}	4.6×10^{7}
Case 2	2.5×10^{16}	3.2	0.08	2.2	0.42	1.4×10^{5}	3.3×10^{7}

Table 7: Debye Length and Mean Free Path Conditions Calculated Assuming Thin Sheath Theory

The Debye length is a few times the radius of the probe, which is outside of the limit for

the thin sheath theory. According to the parameters calculated from the thin sheath theory, the Debye length condition violates the main assumption of the thin sheath analysis. Based on the sheath thickness criteria, neither the thin sheath or Orbit Motion Limit theory of collection would be ideal.

4.2 Implementation of Orbital Motion Limit Theory

The electron saturation region is the portion of the curve with probe voltages greater than the plasma potential. For cylindrical probes, the electron saturation current varies with the square root of the probe voltage as seen in equation (65). Therefore, in the ideal OML case, a plot of the square of the saturation current yields a straight line. In Figure 27 there is no such relationship. Without an electron saturation current, it is impossible to apply the OML theory for electron collection. The OML theory for ion collection is for ion attracting probe voltages. The voltage domain was limited to -2 to 28V in order to reduce the amount of time it takes to make one sweep. Over this range, there was no clear trend in the ion saturation. Figure 35 is a plot of the square of the probe current. A week linear trend is observed over a range from -2V to 2V. This trend is used to apply the OML theory for ion collection, with the reservation that the limited domain may not be sufficient to get a complete representation of the ion saturation region.

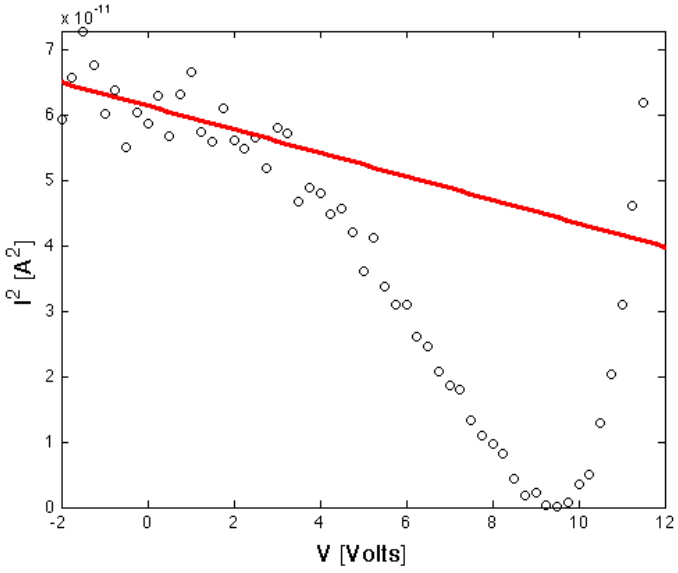

Figure 35: Curvefit for Ion Saturation

The slope of the trendline is used to calculate the ion number density from equation (87).

$$n_i = \sqrt{\frac{d(I_i^2)}{dV_p}} \sqrt{\frac{m_i}{2e}} \frac{\pi}{eA_p} \tag{87}$$

By the quasineutrality condition, the ion density outside the sheath should be approximately equal to the electron density. The electron temperature cannot be determined from the ion collection. The electron temperatures calculated from the thin sheath theory were used for the purposes of calculating the sheath thickness and mean free paths. Although the thin sheath method did not apply, it is used as an approximation. Any other educated guess would have been from a reference on previous experiments. The electron temperature determined from the thin sheath theory is believed to be a better estimate for this cathode than data from previous experiments on other cathodes. Table 8 lists the parameters used to reevaluate the assumptions of the theory.

	n_e (m^{-3})	T_e (eV)	λ_D (mm)	λ_D/r_p	δ (mm)	λ_{ei}/d_p	λ_{en}/d_p
Case 1	2.5×10^{16}	3.4	0.09	2.3	0.43	1.6×10^{5}	3.4×10^{7}
Case 2	6.1×10^{16}	3.2	0.05	1.4	0.27	5.9×10^{4}	1.4×10^{7}

Table 8: Debye Length and Mean Free Path Conditions for OML Theory (T_e From Thin Sheath Theory)

The number density results are on the same order of magnitude as those calculated from the thin sheath theory. The Debye length is again a few times the probe radius. This lies between the boundaries for thin sheath and OML, so neither theory is strictly valid. The mean free paths once again indicate that the plasma is collisionless near the probe. These results are inconclusive since the linear trend in the saturation was not very strong, and the electron temperature from the thin sheath theory has been used. A wider range of sweep voltages is necessary to obtain a clear trend in the ion saturation region.

4.3 Implementation of Druyvesteyn Method

The Druyvesteyn Method offers the flexibility of being used regardless of the sheath size. The first and second derivatives are calculated using the same process used in finding the plasma potential. The probe voltage is measured with respect to facility ground, and the plasma is at the plasma potential, therefore a change of variables is necessary express the electron energy distribution with respect to the plasma potential. This makes the plasma potential the energy reference level, and the voltage V represents the electron energy relative to the plasma potential reference.

$$V = \phi_p - V_p \tag{88}$$

When the probe voltage is well below the plasma potential, only the highest energy electrons reach the probe. As the probe voltage approaches the plasma potential, more lower energy

electrons are collected. A low probe voltage with respect to ground corresponds to a high electron energy with respect to the plasma. The change of variables changes the reference voltage of the probe from facility ground to the plasma potential. The Druyvesteyn equation, which is given in equation (79), is applied with the second derivative of the probe current with respect to the adjusted probe voltage.

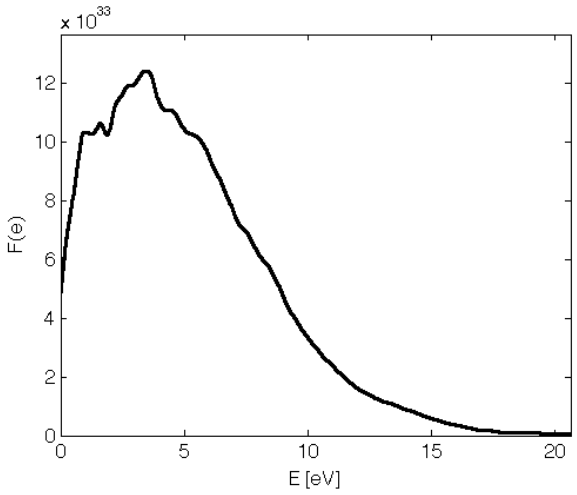

Figure 36: Distribution Function Obtained from Druyvesteyn Method

The number density and electron temperature are obtained from the EEDF according to kinetic theory (equations 80 and 81 in Section 2.7).

$$n_e = \int_0^\infty F(\epsilon) d\epsilon \tag{89}$$

$$T_e = \frac{2}{3}\langle\epsilon\rangle = \int_0^\infty \epsilon F(\epsilon) d\epsilon \tag{90}$$

This process is carried out for each I-V set as the probe passes the cathode. The radial variation of the EEDF and plasma parameters are plotted in Figures 37 and 38. The error in the EEDF measurement and subsequent number density and electron temperature measurements is difficult to predict due to the multiple stages of numerical smoothing and differentiation. Herman and Gallimore[16] estimate an 8% error in determination of the EEDF

by the harmonic method, but do not provide an estimate for the second derivative method. For classical probe theories such as thin sheath and OML, Linell and Gallimore[26] estimate errors of 20% for number density and 50% for electron temperature. While these error values are significant, it is expected that error is relatively consistent across all measurements, and that the trends observed are representative of the true properties of the plume. As discussed in Section 3.4, the uncertainty in the position is ±1.27mm.

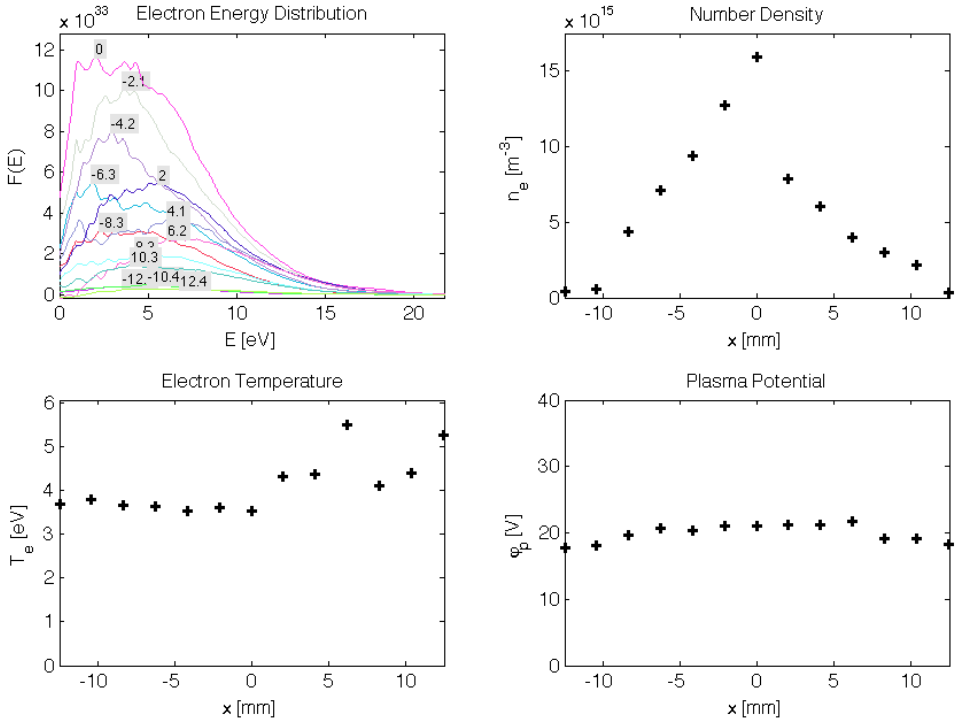

Figure 37: Radial Variation of Plasma Parameters for Case 1

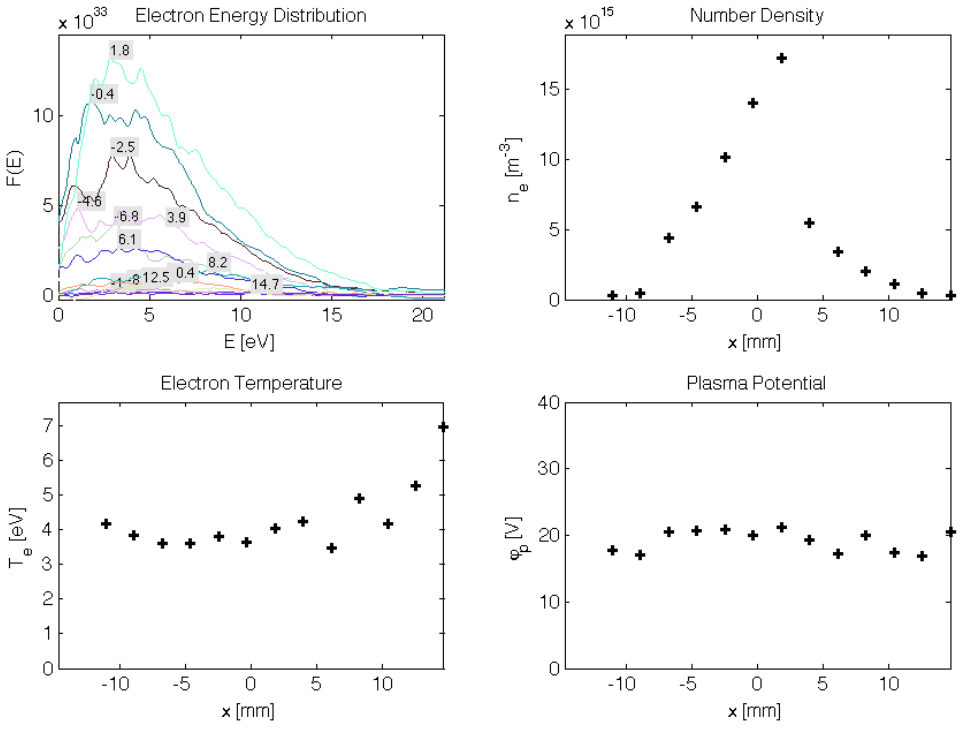

Figure 38: Radial Variation of Plasma Parameters for Case 2

The collisionality assumption was reevaluated based on the plasma properties obtained from the Druyvesteyn Method. At these densities, the plasma is largely collisionless. As seen in Table 9, the mean free paths for electron-ion and electron-neutral interactions are many times larger than the probe dimensions. Sheath thickness and Debye length are omitted from the table, since the Druyvesteyn Method makes no assumptions on sheath thickness.

	n_e (m^{-3})	T_e (eV)	λ_{ei}/d_p	λ_{en}/d_p
Case 1	1.8×10^{16}	4.1	3.1×10^{5}	4.7×10^{7}
Case 2	2.3×10^{16}	4.0	2.3×10^{5}	3.6×10^{7}

Table 9: Mean Free Path Conditions for Druyvesteyn Method

4.4 Results

The Druyvesteyn Method was chosen over the thin sheath and OML analyses because it was the only one of the three that could be properly applied. Results from the Langmuir probe experiment are presented only for the Druyvesteyn Method. The radial variation of the plasma potential is very slight. Figure 39 plots the plasma potential measurements from every pass in both cases. The two plots are nearly indistinguishable. The plasma potential does not exhibit a dependence on the discharge current.

	Case 1	Case 2
I_{anode}	Baseline	133% Baseline

Table 10: Test Conditions

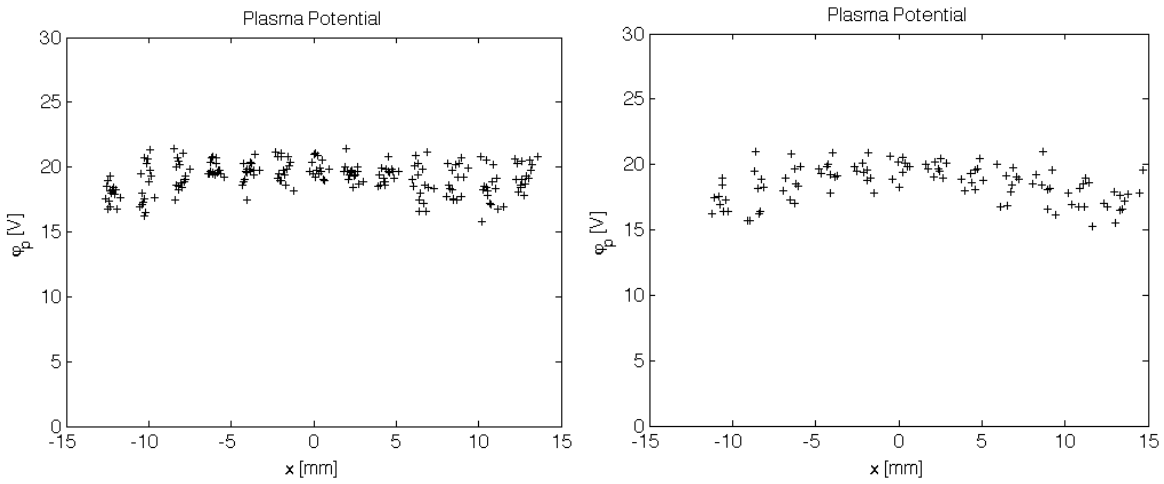

Figure 39: Plasma Potential for Case 1 (left) and Case 2 (right)

The radial variation of electron temperature is plotted in Figure 40. Lower electron temperatures are observed near the center. Case1 has a more distinct trend than case 2. Also, the temperature in the center in Case 2 is higher than in Case 1.

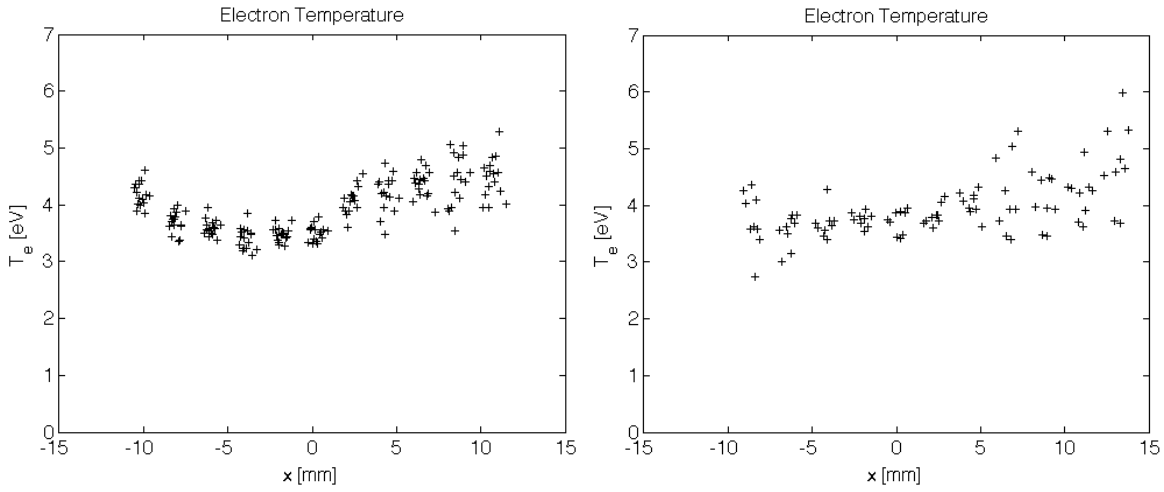

Figure 40: Electron Temperature for Case 1 (left) and Case 2 (right)

Figure 41 shows the number density. Not surprisingly, the number density peaks in the center. Case 2 has a higher peak density in the center than Case 1. The contour is clearly asymmetrical. This is believed to be a result of the anode being misaligned. The cylindrical anode is clamped in place and was not precisely aligned. One side of the anode is closer to the cathode than the other, and it is therefore conceivable that electrons would be more easily drawn to one side.

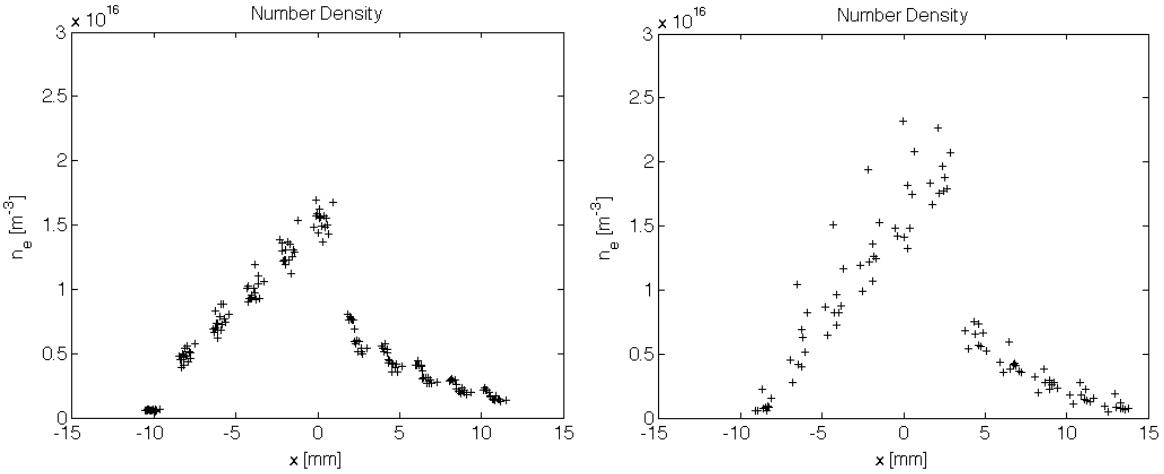

Figure 41: Number Density for Case 1 (left) and Case 2 (right)

The distribution functions obtained from a single I-V curve are too noisy to make a comparison with known functions such as the Maxwellian and Druyvesteyn distributions. The EEDF is obtained while applying as little smoothing as possible in order to preserve important features in the curve. It is possible to use a moving average window that is too large and incur noticeable distortions in the EEDF. With a linear weighting function, excessive smoothing results in a triangular looking curve. To increase the fidelity of the energy distribution, several normalized distribution functions are averaged together. The normalized EEDF is used because it is independent of number density and there is less variability in the normalized EEDF than the non-normalized EEDF. Equations (23) and (32) for the normalized Maxwellian and normalized Druyvesteyn distributions show no dependence on number density. All of the normalized electron energy distribution functions at a specific location are averaged together to generate an averaged normalized EEDF for that location. This averaging process will be referred to as spatial averaging. The repeatability of the position is ± 0.58mm. This incurs additional uncertainty in the position when using spatial averaging. The position uncertainty for the space-averaged EEDF is ± 1.58mm.

Figures 37 and 38 show significant variation in the EEDF. The normalized EEDF, however is much more uniform. The finite repeatability of the position adds additional uncertainty, however this is not a major concern because there is minimal radial variation in the normalized EEDF. The application of the Druyvesteyn Method initially yields the non-normalized EEDF. The normalized EEDF is obtained by dividing the non-normalized EEDF by the number density. Therefore, the determination of the normalized EEDF in practice requires knowledge of the number density, however, the results show no correlation between the normalized EEDF and number density. Figure 42 shows spatially averaged normalized electron energy distribution functions at various radial positions.

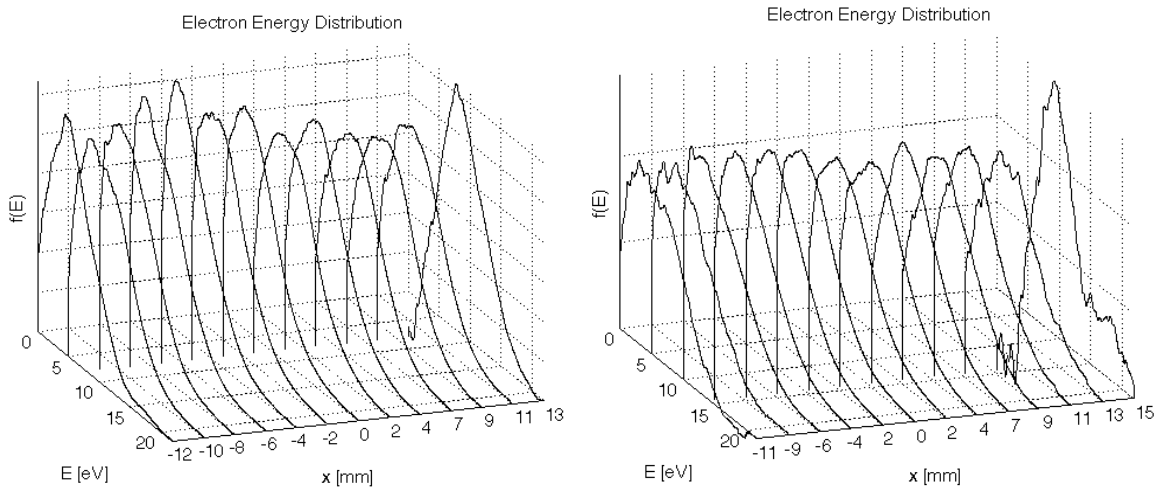

Figure 42: Space-Averaged Radial Variation of Normalized EEDF for Case 1 (left) and Case 2 (right)

Several small peaks are observed to be superimposed on the peak of each distribution, however these peaks are smoothed-out by averaging multiple distributions. Figures 43 and 44 depict the effectiveness of the averaging process and compare the resultant normalized EEDF with the Maxwellian and Druyvesteyn distributions. This averaging process is effective in smoothing the normalized electron energy distribution measurement without applying a more aggressive moving average that would distort the curve.

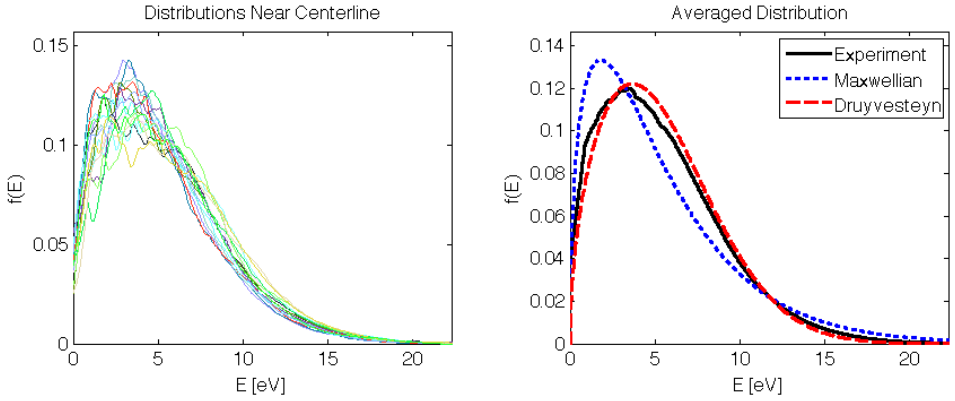

Figure 43: Space-Averaged Normalized EEDF on Axis for Case 1

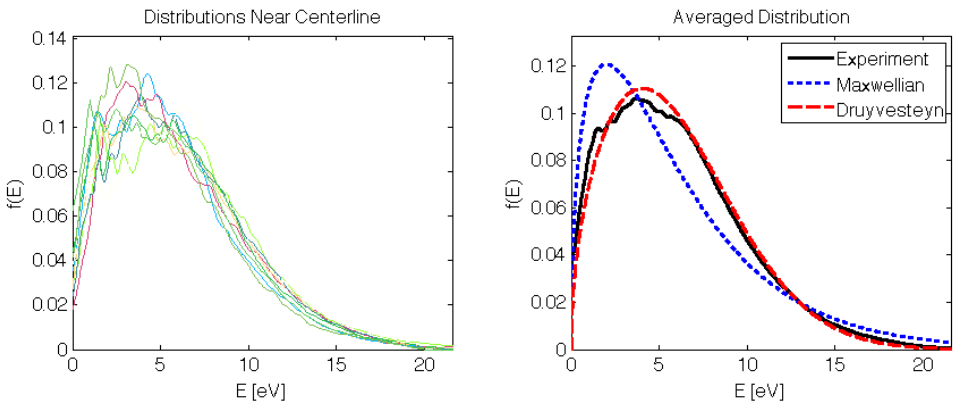

Figure 44: Space-Averaged Normalized EEDF on Axis for Case 2

It is clear that the Druyvesteyn distribution is a better description of the EEDF on axis. Slightly higher energies are more probable in the Druyvesteyn distribution than the Maxwellian. Figure 45 offers a better visualization of the EEDF at various radial locations. Figure 45 represents results from a single pass, that is no spatial averaging has been applied.

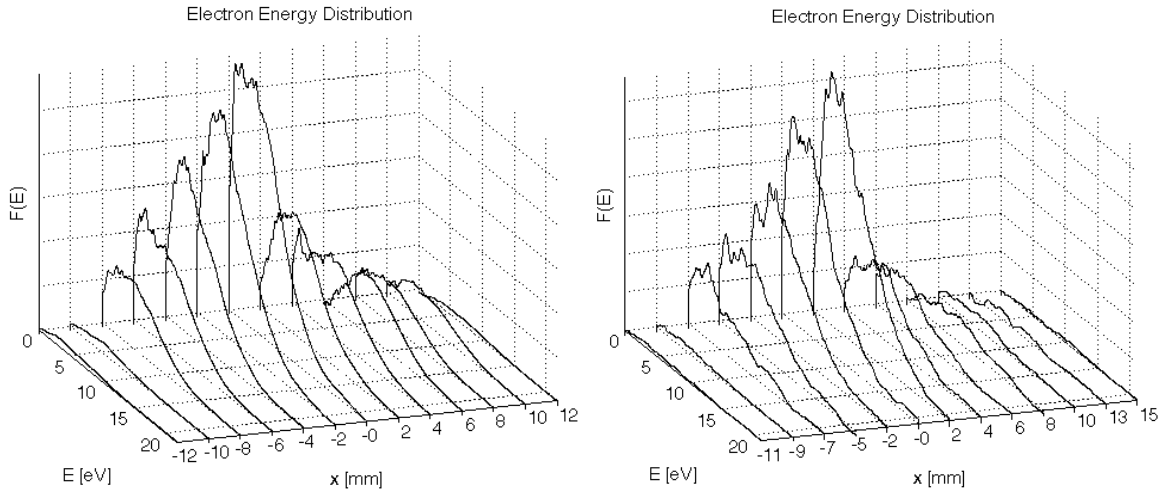

Figure 45: Non-Averaged Radial Variation of Non-Normalized EEDF for Case 1 (left) and Case 2 (right)

The energy distribution functions from all of the passes in each case are then averaged as well. Since the EEDF is not as uniform as the normalized EEDF, the smoothing effect is

more modest. The resulting EEDF profile after spatial averaging is shown in Figure 46.

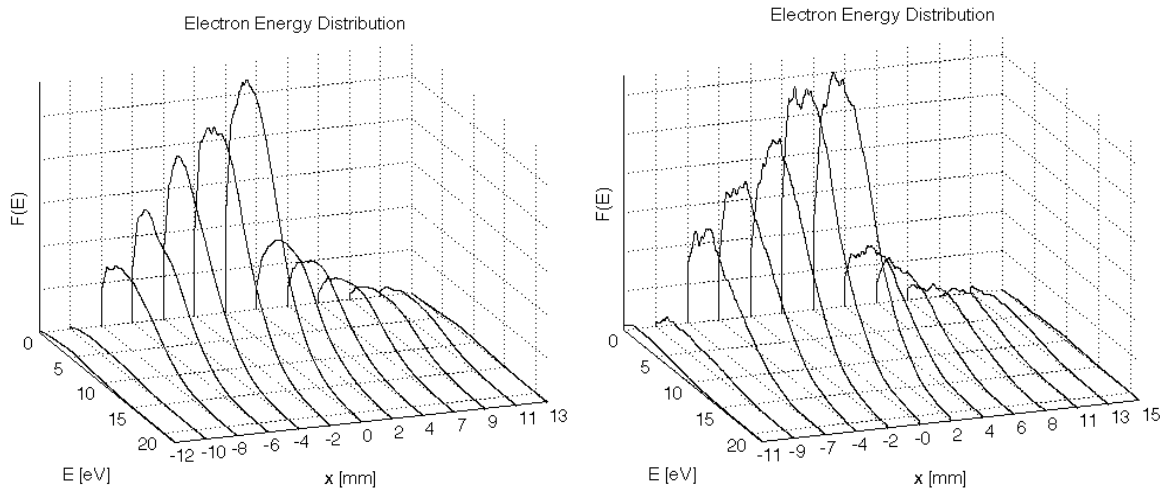

Figure 46: Space-Averaged Radial Variation of non-Normalized EEDF for Case 1 (left) and Case 2 (right)

Although the normalized EEDF is significantly more uniform than the non-normalized one, there exists an interesting trend. The Druyvesteyn distribution provides a good description of the EEDF near the centerline. However there is a increasing deviation from the Druyvesteyn distribution with increasing distance from the centerline, d_r. Several distributions are plotted in Figure 47. The peak of the distribution moves to the right as d_r increases. This is partially a manifestation of the higher electron temperatures off axis, however a second peak in the distribution appears to form off axis as well. Figure 48 further illustrates the off-axis trend.

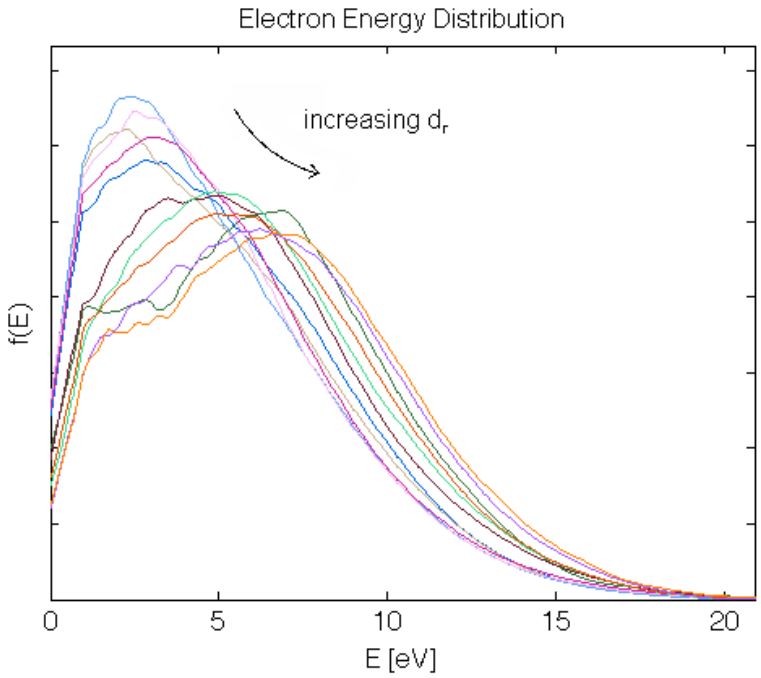

Figure 47: Normalized EEDF at Various Radial Positions

Figure 48 shows the beginnings of the formation of a second peak in the EEDF. The Maxwellian and Druyvesteyn distributions plotted in the figure are for the same mean temperature as the measured distribution. The trend cannot be observed further off axis because the probe current is too low. It is apparent, however that there is an increasing fraction of higher energy electrons off-axis.

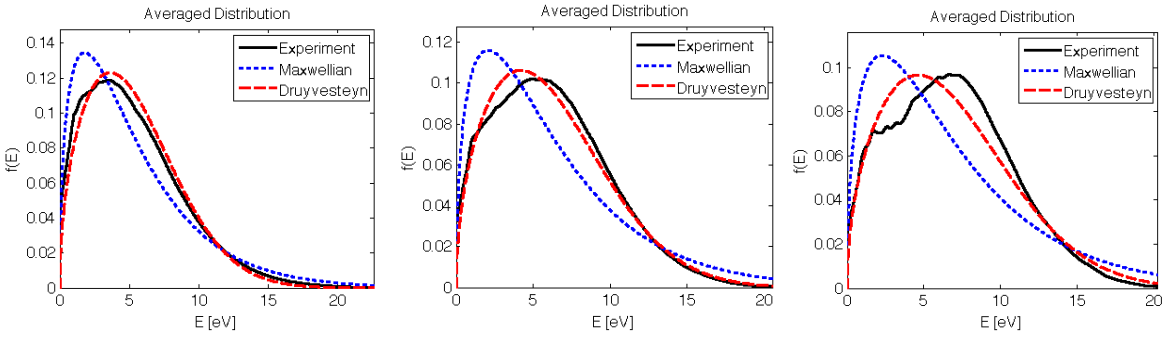

Figure 48: EEDF at d_r=0.0mm (left), d_r=6.5mm (middle) and d_r=10.7mm (right)

Table 11 summarizes the results from each of the three analyses. The values are presented for measurements on axis, directly in front of the cathode. The mean centerline values for number density and electron temperature are listed. Case 2 appears to have a slightly higher electron temperature and number density, and a lower plasma potential than Case 1.

	n_e (m^{-3})	T_e (eV)	ϕ_p (V)
Case 1	1.6×10^{16}	3.7	21.2
Case 2	1.7×10^{16}	3.9	20.2

Table 11: Plasma Parameters for Both Test Cases (x=0 $\pm$1.85mm)

Results indicate that the Druyvesteyn distribution is a better description of the EEDF than the Maxwellian. Despite the fact that the thin sheath theory was invalid for this experiment, it is worth noting that the Druyvesteyn method predicts higher electron temperatures than the thin sheath theory. The Druyvesteyn distribution places more weight on higher electron energies than the Maxwellian, and this is believed to be the reason for the discrepancy in electron temperature since the thin sheath theory assumes a Maxwellian distribution. The average energy, which is directly proportional to the temperature, for a Druyvesteyn distribution is slightly higher than that of the Maxwellian. The thin sheath theory might provide more accurate electron temperatures if it were re-derived assuming a Druyvesteyn distribution. This would involve deriving a modified version of the Botzmann relation.

The asymmetry in the number density with radial position is also observed in the electron temperature. In locations where the number density is low, the electron temperature is high. This is observed in both cases. This indicates the asymmetry is real and not the result of error. The anode, which surrounds the cathode, is not precisely aligned, that is the anode is closer to the cathode on one side than the other.The asymmetrical distribution of the plasma

parameters is attributed to the misalignment of the anode.

The electron temperature is higher off axis than in the center. This is a result of the anode geometry. Electrons in the plume are accelerated radially toward the anode. Faster electrons are found closer to the anode. If the electrons are accelerated to a speed comparable to the thermal speed, the energy distribution function is altered. The deviation of the EEDF from the Druyvesteyn distribution for measurements off axis support the argument that the drift velocity of the electrons is comparable to the thermal speed. The peak of the distribution occurs at higher energies in the measurements further away from the centerline. The beginnings of the formation of a second peak are observed, and it is expected that if the EEDF could be measured further off-axis, it would reveal a double-peak distribution. For this reason, the electron temperature measurements off axis are invalid. It is more likely that the electron temperature is relatively constant, and the radial variation that is observed is an manifestation of the electron drift velocity.

While this experiment provides a detailed description of the behavior of the electrons in the plume, it does not provide any information on the ion and neutral populations. Data on the heavy species temperature and electron drift velocity in hollow cathodes from previous work is used for the purpose of estimation. Goebel[2] provides information for the NEXIS cathode that can be used to develop a broader understanding of the characteristics of the plume region plasma. The ion temperature is approximately equal to the neutral temperature and is assumed to be one tenth the electron temperature and the electron drift velocity is approximately 65% of the electron thermal speed.[2] These values are used with the acknowledgement that there are many factors that could introduce variability between the NEXIS cathode and the BHT-1500. Assuming the same electron to ion temperature ratio and relative electron drift velocity as in Goebel,[2] the drift velocities for each species can be estimated. The thermal velocity of each species is calculated from the temperature,

assuming the velocity distribution is Maxwellian.

$$v_{th} = \sqrt{\frac{8kT}{\pi m}} \tag{91}$$

As stated in Section 3.3, the ion and neutral drift velocity is estimated by assuming a neutral continuum fluid and that the flow in the cathode orifice is choked. Using an electron temperature of 1.36 eV for the insert region[2], and again assuming the heavy species temperature is one tenth the electron temperature, the speed of sound is calculated. This value represents the drift velocity for ions and neutrals. Tables 12 and 13 summarize the basic physical characteristics for each population using the same assumptions in Goebel[2] for the ion to electron temperature ratio and relative electron drift velocity.

$$a = \sqrt{\gamma RT} \tag{92}$$

	n (m^{-3})	T (eV)	v_{drift} (m/s)	v_{th} (m/s)
Electrons	1.6×10^{16}	3.7	8.4×10^5	1.3×10^6
Ions	1.6×10^{16}	0.37	7.4×10^2	1.5×10^3
Neutrals	1.6×10^{16}	0.37	7.4×10^2	1.5×10^3

Table 12: Properties of Different Species on Centerline (Case 1)

	n (m^{-3})	T (eV)	v_{drift} (m/s)	v_{th} (m/s)
Electrons	1.7×10^{16}	3.9	8.6×10^5	1.3×10^6
Ions	1.7×10^{16}	0.39	7.4×10^2	1.6×10^3
Neutrals	1.7×10^{16}	0.39	7.4×10^2	1.6×10^3

Table 13: Properties of Different Species on Centerline (Case 2)

The estimate for electron drift velocity may be too high. The EEDF measured at the centerline does not indicate a substantial drift velocity. The number density of each species is assumed to be uniform. This is consistent with Goebel's[2] values for electron and neutral density at 1.0 cm from the keeper orifice.

The frequencies of different interactions also provide insight into the characteristics of the plume. The frequencies of several elastic and inelastic collisions are determined based on the electron temperature and number density measured at the centerline, as well as tabulated cross section data. The electron-ion cross section is calculated as described in Section 2.4.2. The ion-neutral cross sections are determined based on the hard-sphere model (also described in Section 2.4.2). The elastic electron-neutral, inelastic electron-neutral(ionization) and inelastic ion-neutral (charge-exchange) cross sections are tabulated by Mitchner and Kruger.[35] The ionization cross section is negligible, as the electron temperatures for these tests were all in the 3 to 4 eV range, below the ionization energy threshold for argon of 15.8 eV. Also, the data available provides ion-neutral charge-exchange cross sections for ion energies only as low as 3 eV. For the purpose of estimation, the cross section corresponding to the lowest tabulated ion energy is used in determining the cross section for ion-neutral charge-exchange collisions. The cross sections are used to determine the corresponding collision frequencies according to equation (93).[36] The expression in equation (93) for collision frequency in a partially ionized gas implies that all particles have a Maxwellian distribution and that the electron temperature is much greater than the ion temperature.[36] The cross section values used for ion-neutral charge-exchange collisions presumably results in an underestimation of the frequency of such interactions.

$$\nu = \frac{n\sigma v_{th}}{\sqrt{2}} \tag{93}$$

The mean free path for a particular species is determined by dividing the thermal velocity by the sum of the collision frequencies involving that species.[36] For example, the mean free path

for neutrals is equal to the thermal velocity of the neutral population divided by the sum of the collision frequencies for electron-neural, ion-neutral, and charge exchange interactions.

$$\lambda_n = \frac{v_{th_n}}{\nu_{en} + \nu_{in} + \nu_{in(CEX)}} \tag{94}$$

Tables 15, 16 and 14 summarize the collisional properties of the plasma for several interactions.

	Electron-Neutral	Ion-Neutral	Electron-Ion	Ionization	Charge-Exchange
Case 1	2.1×10^{-19}	6.3×10^{-20}	2.9×10^{-18}	-	4.0×10^{-19}
Case 2	2.25×10^{-19}	6.3×10^{-20}	2.6×10^{-18}	-	4.0×10^{-19}

Table 14: Cross Sections for Various Interactions [m^2]

	Electron-Neutral	Ion-Neutral	Electron-Ion	Ionization	Charge Exchange
Case 1	3.1×10^3	1.01	4.2×10^4	-	6.87
Case 2	3.9×10^3	1.18	4.1×10^4	-	7.49

Table 15: Collision Frequencies for Various Interactions [s^{-1}]

	Electrons	Ions	Neutrals
Case 1	147	3.3	50
Case 2	153	3.4	44

Table 16: Mean Free Paths for Different Species [cm]

The thermal velocity of the electrons is used to evaluate the collision frequencies of interactions involving an electron. In the other cases, the thermal velocity of the heavy

species is used. The mean free paths for each species is on the order of centimeters, and much larger than the dimensions of the plume with the exception of the ion mean free path. The ion mean free path is 3.3 cm in Case 1, and the diameter of the cylindrical anode is 7.6 cm. Since the collision frequency for electron-ion collisions is much greater than it is for ion-neutral, it follows that ion collisions are mainly with electrons. It is reasonable to deduce that the most frequent collisions in the plume occur between electrons and ions. It is conceivable that the number density closer to the keeper orifice is greater than it is at a distance of 1.0 cm, and collisions are more frequent.

5 Conclusions and Recommendations

Determination of the plasma potential is essential in all of the analyses performed. Specifically, in the Druyvesteyn method, the plasma potential affects the low energy region of the distribution function and consequently impacts the number density and electron temperature calculations. When the reference change is made by applying $V = \phi_p - V_p$ the plasma potential becomes the zero energy reference point, and EEDF shifted on the horizontal axis. In the ideal case, the second derivative is equal to zero for probe voltages greater than the plasma potential, however in practice this is not the case. Data collected when the probe potential is greater than the plasma potential is not used in the Druyvesteyn method because it theoretically would correspond to electrons with energies less than zero. Put differently, the plasma potential represents a minimum cutoff value in the domain of the EEDF. An error in the plasma potential shifts the EEDF, affecting the electron temperature, and changes the area under the curve and consequently the number density. Chen[31] states that I-V curves that do not have the traditional shape can be obtained at very low plasma densities. The lack of a well-defined knee is believed to be due to the low density. Since this is an otherwise unremarkable dc plasma with no magnetic fields present, this is the most likely explanation. In cases where the I-V curve lacks a well-defined knee, a supplemental emissive probe diagnostic would be well-advised to provide an independent measurement of the plasma potential.

The collision frequencies at a distance of 1.0 cm from the keeper orifice indicate that the plume region of the plasma is largely collisionless. An electron exits the cathode with an energy ϵ and has a low probability of interacting with another particle in the plume. It follows that the EEDF is relatively uniform in the axial direction, as there are not enough collisions taking place to alter it. Since there are so few collisions in the plume region, it is likely that the EEDF is determined by the characteristics of the orifice region plasma

and the ambient electric field outside the cathode. If a non-equilibrium EEDF exists in the orifice region, it is possible that the there are not enough collisions taking place to restore the EEDF to equilibrium.

The speed with which the Sourcemeter makes I-V sweeps is relatively slow compared to the transit time. This makes applying the Druyvesteyn method more difficult. More data points on each probe characteristic would allow more aggressive smoothing, making differentiation less likely to introduce noise. Also, if the sampling frequency of the probe data was increased, the probe could be moved through the plasma faster.

The Orbital Motion Limited collection theory cannot be properly applied. No electron saturation is observed, and there is no compelling trend observed in the ion saturation within the voltage domain examined. It may be beneficial to perform a test with an expanded voltage domain to try to capture an ion saturation current.

The positioning system moves very slowly as well. If the positioning system were upgraded or replaced, it would allow for faster, less obtrusive interrogation of the plume, and would reduce the heat transfer to the probe during each pass. With a faster moving probe, it would be possible to characterize the plume closer to the orifice.

While the probe position is known to a reasonable accuracy, the low repeatability is detracting. Averaging multiple measurements in the same location improves results. This technique was applied at the expense of added position uncertainty. It would be beneficial to eliminate this additional uncertainty with an improved positioning system.

Of the three analyses, the Druyvesteyn method is the most robust because it's validity is independent of the sheath size. Also, the determination of the EEDF provides a more detailed description of the plasma. Based on the centerline number density and electron temperature, neither the thin sheath or OML theories were well suited for this application because of the Debyle length criteria (described in Section 2.4.1) that must be satisfied. The OML theory was only valid in the lower density regions off axis. The Druyvesteyn method

presents different challenges because the second derivative of the probe characteristic is required. The method requires as clean a signal as possible, and smoothing must be applied with discretion. When applied correctly, the Druyvesteyn method is a powerful tool.

References

[1] G. P. Sutton and O. Biblarz, *Rocket Propulsion Elements*. Wiley, 7 ed., 2001.

[2] D. Goebel and I. Katz, *Fundamentals of Electric Propulsion: Ion and Hall Thrusters*. Wiley, 2008.

[3] I. Katz, I. Mikellides, and D. Goebel, "Model of the plasma potential distribution in the plume of a hollow cathode," *40 th Joint Propulsion Conference*, pp. 2004–4108.

[4] I. Katz, I. Mikellides, D. Goebel, K. Jameson, R. Wirz, and J. Polk, "Production of high energy ions near an ion thruster discharge hollow cathode," 2006.

[5] A. Grill, *Cold Plasma Materials Fabrication: From Fundamentals to Applications*. Wiley, 1994.

[6] J. Bittencourt, *Fundamentals of Plasma Physics*. Pergamon Press, 1986.

[7] J. Allen, "Probe theory- the orbital motion approach," *Physica Scripta*, vol. 45, no. 5, pp. 497–503, 1992.

[8] K. J. T. Paul M. Chung, Lawrence Talbot, *Electric Probes in Stationary and Flowing Plasmas: Theory and Application*. Springer-Verlag, 1975.

[9] K. Jameson, D. Goebel, and R. Watkins, "Hollow cathode and keeper-region plasma measurements using ultra-fast miniature scanning probes," *AIAA Paper*, vol. 3667, p. 41, 2005.

[10] F. F. Chen, *Introduction to Plasma Physics and Controlled Fusion*, vol. 1: Plasma Physics. Plenum Press, 1984.

[11] A. Sengupta, J. Brophy, and K. Goodfellow, "Wear characteristics from the extended lift test of the ds1 flight spare ion thruster," *28th International Electric Propulsion Conference*, 2003.

[12] D. Goebel, K. Jameson, I. Katz, and I. Mikellides, "Energetic ion production and keeper erosion in hollow cathode discharges," *IEPC*, pp. 1–18, Oct 2005.

[13] I. K. D. G. K. J. I. Mikellides, "Driving processes in the orifice and near-plume regions of a hollow cathode," *AIAA*, pp. 1–16, Sep 2006.

[14] I. Langmuir, "The interaction of electron and positive ion space charges in cathode sheaths," *Langmuir Phys Rev*, vol. 33, p. 954, 1913.

[15] G. Williams, T. Smith, and A. Gallimore, "Fmt-2 discharge cathode erosion rate measurements via laser induced fluorescence," *AIAA Paper*, vol. 3663, 2000.

[16] D. Herman and A. Gallimore, "Discharge cathode electron energy distribution functions in a 40-cm next-type ion engine," *41st Joint Propulsion Conference, AIAA-2005-4252*, 2005.

[17] V. Godyak, R. Piejak, and B. Alexandrovich, "Measurement of electron energy distribution in low-pressure rf discharges," *Plasma Sources Science and Technology*, vol. 1, pp. 36–58, 1992.

[18] V. Godyak, "Measuring eedf in gas discharge plasmas," *NATO ASI series. Series E, Applied sciences*, vol. 176, pp. 95–134, 1990.

[19] M. Hopkins and W. Graham, "Langmuir probe technique for plasma parameter measurement in a medium density discharge," *Review of Scientific Instruments*, Jan 1986.

[20] K. U. Sawlani and J. E. Foster, "Comparison of various numerical schemes to obtain eedf with high accuracy," *31st International Electric Propulsion Conference*, Oct 2009.

[21] J. Walter G. Vincenti, Charles H. Kruger, *Introduction to Physical Gas Dynamics*. Krieger Publishing Company, 1965.

[22] M. Druyvesteyn and F. Penning, "The mechanism of electrical discharges in gases of low pressure," *Reviews of Modern Physics*, vol. 12, no. 2, pp. 87–174, 1940.

[23] M. Li, S. Dew, and M. Brett, "Effects of electron distribution functions on the floating potential of particles in the plasma: thin plasma sheaths," *Journal of Physics D: Applied Physics*, vol. 32, pp. 2056–2059, 1999.

[24] A. J. L. Michael A. Lieberman, *Principles of Plasma Discharges and Materials Processing*. Wiley, 2005.

[25] N. Hershkowitz, "How langmuir probes work," *Plasma Diagnostics*, pp. 1–72, May 1989.

[26] J. Linnell and A. Gallimore, "Internal langmuir probe mapping of a hall thruster with xenon and krypton propellant," 2006.

[27] J. Laframboise and L. Parker, "Probe design for orbitlimited current collection," *Physics of Fluids*, vol. 16, p. 629, 1973.

[28] F. Chen, "Electric probes," *Plasma diagnostic techniques*, p. 113, 1965.

[29] V. Demidov, S. Ratynskaia, and K. Rypdal, "Electric probes for plasmas: The link between theory and instrument," *Review of scientific instruments*, vol. 73, p. 3409, 2002.

[30] B. Lipschultz, I. Hutchinson, B. LaBombard, and A. Wan, "Electric probes in plasmas," *Journal of Vacuum Science & Technology A: Vacuum, Surfaces, and Films*, vol. 4, p. 1810, 1986.

[31] F. Chen, "Langmuir probe diagnostics," *Mini-Course on Plasma Diagnostics, IEEE-ICOPS Meeting, Jeju, Korea*, 2003.

[32] V. Godyak, R. Piejak, and B. Alexandrovich, "Probe diagnostics of non-maxwellian plasmas," *J. Appl. Phys.*, vol. 73, p. 3657, 1993.

[33] S. Writers, "The first us hall thruster is operational in space," March 2007.

[34] E. Fossum, J. Sommerville, and L. King, "Characterization of near field plasma environment of a hollow cathode assembly," *40 th AIAA/ASME/SAE/ASEE Joint Propulsion Conference and Exhibit*, 2004.

[35] M. Mitchner and J. C. H. Kruger, *Partially Ionized Gases*. John Wiley and Sons, 1973.

[36] D. Hastings and H. Garrett, *Spacecraft-Environment Interactions*. Cambridge University Press, 2004.

A MATLAB Programs

A.1 Plasma Potential

```
function [phi_p]=phi_func(data, phi_min,phi_max,window,order)

%% Import Data
V=data(:,1);
I=data(:,2);
x=data(:,3);

I=I-1.1*min(I);
%calculate dV
for i=1:length(V)-1, dV(i)=V(i+1)-V(i); end
dV=mean(dV);
n=(max(V)-min(V))/dV;

%spline
V_old=V;
I_old=I;
dV=dV/10;
V=min(V_old):dV:max(V_old);
I = spline(V_old,I_old,V);

%curvefit
V1=10;
V2=14;
V3=24;
V4=27.5;

[a,cut1]=min(abs(V-V1));
[a,cut2]=min(abs(V-V2));
[a,cut3]=min(abs(V-V3));
[a,cut4]=min(abs(V-V4));

I_2=I(cut1+1:cut2);        V_2=V(cut1+1:cut2);
I_4=I(cut3+1:cut4);        V_4=V(cut3+1:cut4);

lnI=log(I);
lnI_2=log(I_2);
```

```
lnI_4=log(I_4);

coeff3=polyfit(V_2,lnI_2,1);     linfit3=coeff3(1)*V+coeff3(2);
coeff4=polyfit(V_4,lnI_4,1);     linfit4=coeff4(1)*V+coeff4(2);

%% Differentiate I(V)
I=smooth(I,window,'sgolay',order);
for i=2:length(V)-1
   dI(i)=(I(i+1)-I(i-1))/2/dV;
end

i=1; dI(i)=(-3*I(i)+4*I(i+1)-I(i+2))/2/dV;
i=length(V); dI(i)=(3*I(i)-4*I(i-1)+I(i-2))/2/dV;


%% Differentiate dI(V)/dV
dI=smooth(dI,window,'sgolay',order);
for i=2:length(V)-1
   dI2(i)=(dI(i+1)-dI(i-1))/2/dV;
end

i=1; dI2(i)=(-3*dI(i)+4*dI(i+1)-dI(i+2))/2/dV;
i=length(V); dI2(i)=(3*dI(i)-4*dI(i-1)+dI(i-2))/2/dV;

dI2=smooth(dI2,window/2,'sgolay',order);

%% Plasma Potential
[a,cut3]=min(abs(V-phi_min));
[a,cut4]=min(abs(V-phi_max));
V_sub=V(cut3:cut4);
dI_sub=dI(cut3:cut4);
dI2_sub=dI2(cut3:cut4);
[pks,locs] = findpeaks(dI_sub);
[pks2,locs2] = findpeaks(-dI2_sub,'sortstr','descend');
if length(pks2)>3
pks2=pks2(1:3);
locs2=locs2(1:3);
end
[a,cut7]=min(abs(linfit3-linfit4));
iphi=cut7;
bool=isempty(locs);
bool2=isempty(locs2);
```

```
if bool==0
    for i=1:length(pks)
       V_pks(i)=V_sub(locs(i));
    end
   [pk,maxloc]=min(abs(V_pks-round(mean([phi_min,phi_max]))));
   cut8=locs(maxloc)+cut3;
   iphi=round(mean([cut7,cut8]));
end
if bool2==0
    for i=1:length(pks2)
       V_pks2(i)=V_sub(locs2(i));
    end
   [pk2,minloc]=min(abs(V_pks2-round(mean([phi_min,phi_max]))));
   cut6=locs2(minloc)+cut3;
   iphi=round(mean([cut6,cut7]));
end
if bool==0 && bool2==0
iphi=round(mean([cut6,cut7,cut8]));
end

phi_p=V(iphi);
```

A.2 Thin Sheath Theory

```
function [ne,Te,phi_p,xcoord]=thin_func(data)
%% Introduce Constants, Import Data
e=1.60217646e-19;               %Elementary Charge [Coulombs]
k=1.3806503e-23;                %Boltzmann Constant
e_o=8.854187e-12;               %Permittivity of Freespace
m_e=9.10938188e-31;             %Mass of electron [kg]
M=6.62e-26;                     %Mass of Argon atom [kg]
D_p=.003*.0254;                 %Probe Diameter [m]
L_p=.002;                       %Probe Length [m]
A_p=pi*D_p*L_p+pi*D_p^2/4;      %Probe Area
r_p=D_p/2;                      %Probe Radius

V=data(:,1);
I=data(:,2);
x=data(:,3);
```

```
%obtain plasma potential
phi_min=15;
phi_max=25;
[phi_p]=phi_func(data, phi_min,phi_max,120,1);

xcoord=mean(x);
dx=abs(max(x)-min(x));
I_orig=I;
%generate linear curvefit for ion current, subtract from total current
[a,cutf]=min(abs(I));
V_f=V(cutf);
[a,cut0]=min(abs(V-(V_f-3)));
I_i=I(3:cut0);              V_i=V(3:cut0);
coeffi=polyfit(V_i,I_i,1);
Ii_sat=coeffi(1)*V+coeffi(2);
I=I-min(I);
lnI=log(I);

%% Split Into Sections
V1=5;
V2=phi_p-4;

[a,cut1]=min(abs(V-V1));
[a,cut2]=min(abs(V-V2));

I_2=I(cut1+1:cut2);         V_2=V(cut1+1:cut2);
lnI_2=log(I_2);

coeff3=polyfit(V_2,lnI_2,1);     linfit3=coeff3(1)*V+coeff3(2);

%% Determine Plasma Parameters
Te=1/coeff3(1);
[a,i_phi]=min(abs(V-phi_p));
i_phi=i_phi;
C_bar=2*sqrt(2*e*Te/m_e/pi);
ne=4*exp(linfit3(i_phi))/e/C_bar/A_p;
```

A.3 Druyvesteyn Method

```
function [phi_p, xcoord, F, f, V, ne, Te, V_f]=druy_func2(data, phi_min,phi_max,window,o

%% Introduce Constants, Import Data
e=1.60217646e-19;               %Elementary Charge [Coulombs]
k=1.3806503e-23;                %Boltzmann Constant
e_o=8.854187e-12;               %Permittivity of Freespace
m_e=9.10938188e-31;             %Mass of electron [kg]
m_ar=6.62e-26;                  %Mass of Argon atom [kg]
D_p=.003*.0254;                 %Probe Diameter [m]
L_p=.002;                       %Probe Length [m]
A_p=pi*D_p*L_p+pi*D_p^2/4;      %Probe Area
r_p=D_p/2;                      %Probe Radius

V=data(:,1);
I=data(:,2);
x=data(:,3);
flow=data(:,4);
P=data(:,5);
V_k=data(:,6);
I_k=data(:,7);
V_a=data(:,8);
I_a=data(:,9);

xcoord=mean(x);
dx=abs(max(x)-min(x));

%calculate dV
for i=1:length(V)-1, dV(i)=V(i+1)-V(i); end
dV=mean(dV);
n=(max(V)-min(V))/dV;

V_old=V;
I_old=I;
dV=dV/10;
V=min(V_old):dV:max(V_old);
I = spline(V_old,I_old,V);

%% Differentiate I(V)
I=smooth(I,window,'sgolay',order);
```

```
for i=2:length(V)-1
   dI(i)=(I(i+1)-I(i-1))/2/dV;
end

i=1; dI(i)=(-3*I(i)+4*I(i+1)-I(i+2))/2/dV;
i=length(V); dI(i)=(3*I(i)-4*I(i-1)+I(i-2))/2/dV;


%% Differentiate dI(V)/dV
dI=smooth(dI,window,'sgolay',order);
for i=2:length(V)-1
   dI2(i)=(dI(i+1)-dI(i-1))/2/dV;
end

i=1; dI2(i)=(-3*dI(i)+4*dI(i+1)-dI(i+2))/2/dV;
i=length(V); dI2(i)=(3*dI(i)-4*dI(i-1)+dI(i-2))/2/dV;


%% Store Plasma Parameters
[phi_p]=phi_func(data, phi_min,phi_max,120,1);
[a,cut5]=min(abs(V-phi_p));
dI2(cut5+1)=0;
[a,ifloat]=min(abs(I));
V_f=V(ifloat);
V_p=V;
V=0:dV:max(V);
dI2(cut5+1:length(V))=0;
dI2=smooth(dI2,round(window/2),'sgolay',order);
dI2=dI2(1:cut5+1);
dI2(1)=0;
dI2=flipud(dI2);
dI2(cut5+1:length(V))=0;
dI2=flipud(dI2);

%Calculate F(e)
for i=1:length(V)
F(i)=4/e^2/A_p*sqrt(m_e*V(i)/2/e)*dI2(i);
end
F=fliplr(F);
F(length(F):length(V))=0;
% Integrate distribution to determine density and electron temp
ne=0; E_avg=0;
```

```
for i=1:length(V)
    ne=ne+e*dV*F(i);                    %Number density [m^-3]
    E_avg=E_avg+e*V(i)*e*dV*F(i);       %Avg Energy [Joules]
end
f=F/ne*e;                               %Normalized Distribution
Te=2/3*E_avg/ne/e;                      %Te [eV]
```

B LabVIEW Programs

B.1 Data Acquisition Program

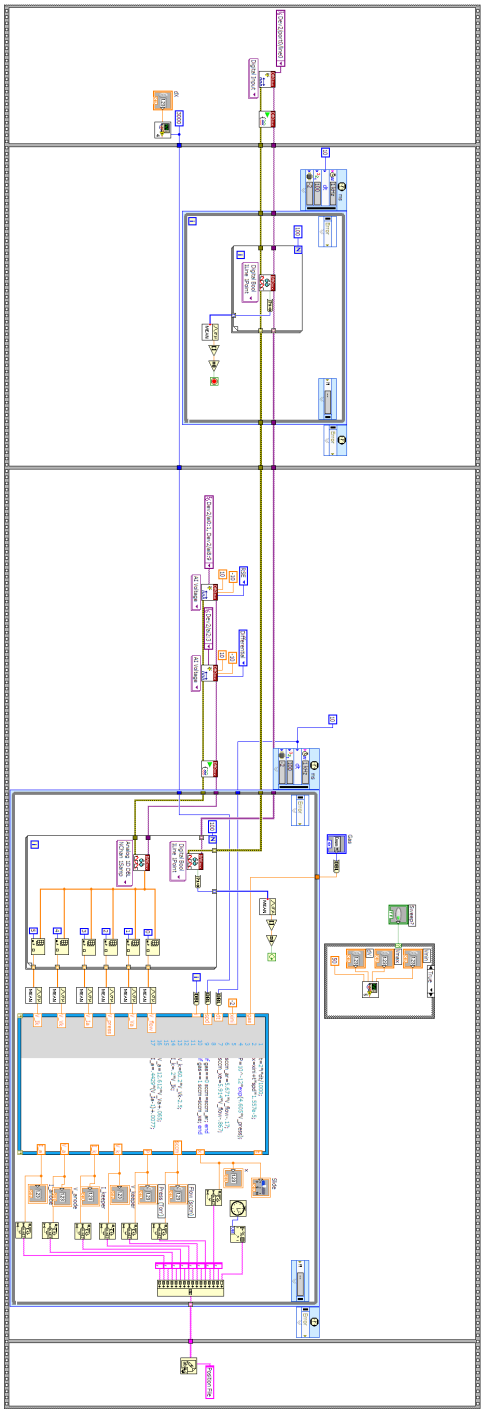

B.2 Sourcemeter Control Program

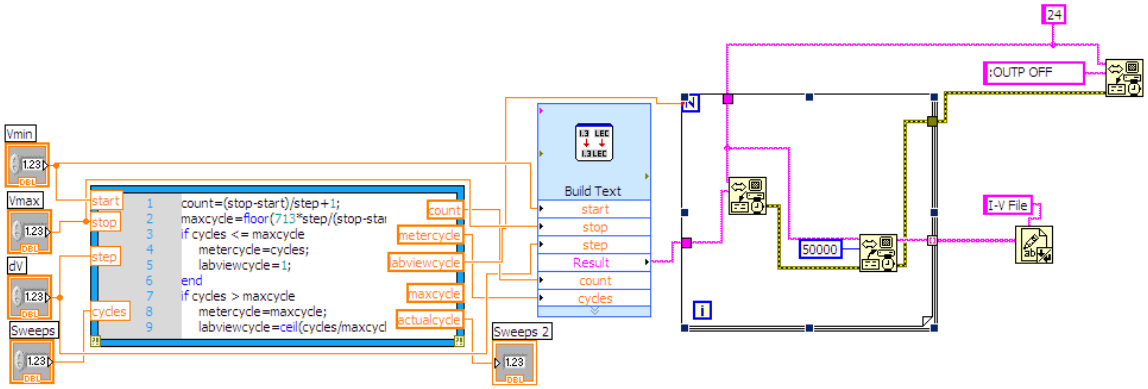

B.3 Position Control Program

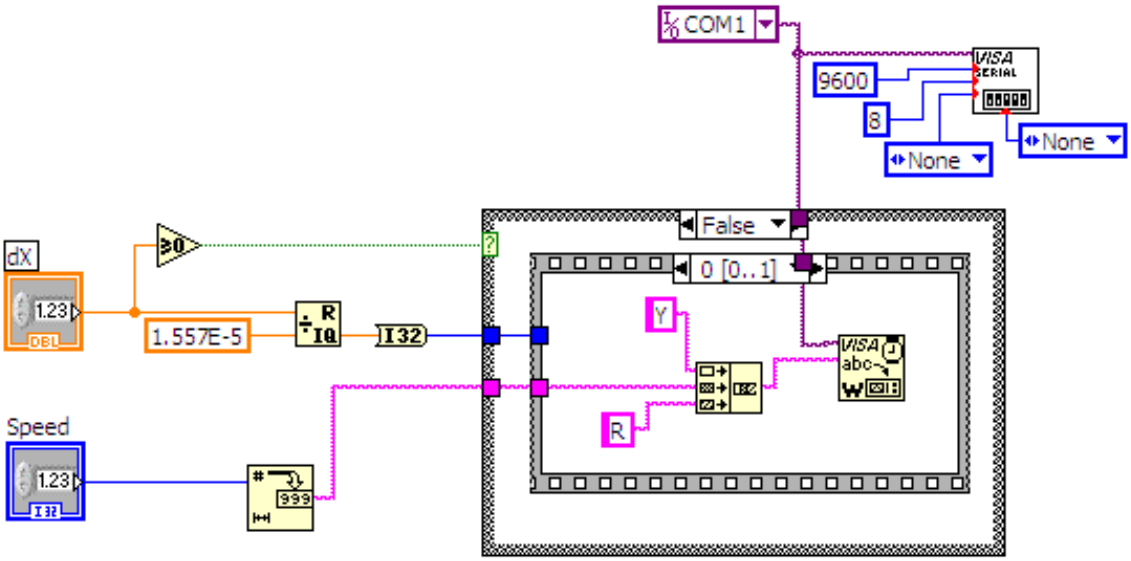

C Mean Free Path Derivation for Coulomb Interaction

The derivation to be presented is a summary of the one published by Bittencourt.[6] First, consider two charged particles that are not on a direct collision course. The geometry and coordinate system for the interaction is shown in Figure 49.

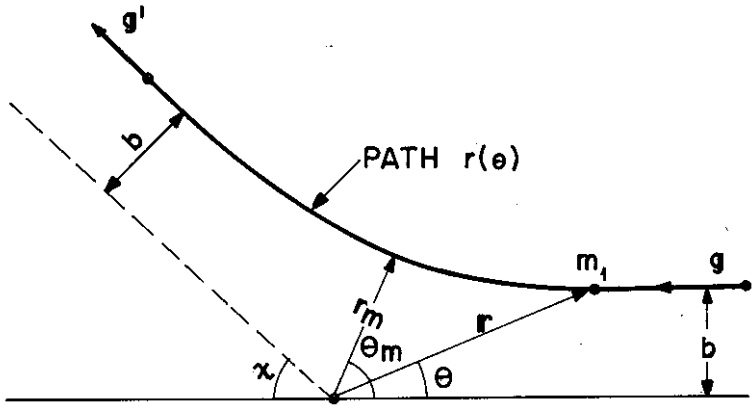

Figure 49: Collision Coordinates[6]

The incident particle m_1 approaches the target particle m with relative velocity g and impact parameter b, and is scattered through an angle χ. The total energy of motion is

$$E = \frac{\mu g^2}{2} \tag{95}$$

where the reduced mass, $\mu = \frac{mm_1}{m+m_1}$

The kinetic energy of the relative motion during the interaction is

$$K = \frac{1}{2}\mu\left(\dot{r}^2 + r^2\dot{\theta}^2\right) \tag{96}$$

The total energy then be written as the sum of the kinetic energy in equation (96) and potenial energy $\phi(r)$.

$$\frac{1}{2}\mu\left(\dot{r}^2 + r^2\dot{\theta}^2\right) + \phi(r) = \frac{\mu g^2}{2} \tag{97}$$

By conservation of angular momentum,

$$\mu r^2 \dot{\theta} = b\mu g \tag{98}$$

The differential equation for the orbit can be written based on conservation of energy and angular momentum.

$$\frac{\partial r}{\partial t} = \frac{\partial r}{\partial \theta}\frac{\partial \theta}{\partial t} \tag{99}$$

From equations 97 and 98 the following substitutions are made

$$\frac{\partial \theta}{\partial t} = \frac{bg}{r^2} \tag{100}$$

$$\frac{\partial r}{\partial t} = \sqrt{2\left(\frac{1}{2}\mu g^2 - \phi(r)\right)\mu - r^2\dot{\theta}^2} \tag{101}$$

The result of the substitution is a differential equation of motion.

$$\frac{\partial r}{\partial \theta} = \pm\frac{r^2}{b}\sqrt{1 - \frac{b^2}{r^2} - \frac{2\phi(r)}{\mu g^2}} \tag{102}$$

As seen in Figure 49, the trajectory of particle m_1 is symmetrical with respect to the apse line r_m, which corresponds to the distance of closest approach. The positive solution to (102) is used when $\theta > \theta_m$, while the negative solution is for $\theta < \theta_m$. At closest approach $dr/d\theta = 0$, and it is possible to write expressions for the distance of closest approach.

$$r_m = b\left(1 - \frac{2\phi(r_m)}{\mu g^2}\right)^{-\frac{1}{2}} \tag{103}$$

The orientation of the apse line is obtained by integrating (102).

$$\theta_m = \int_{r_m}^{\infty} \frac{b}{r'^2}\left[1 - \frac{b^2}{r'^2} - \frac{2\phi(r')}{\mu g^2}\right]^{-\frac{1}{2}} dr' \tag{104}$$

Referring again to Figure 49, the scattering angle is the supplement of twice the apse line angle.

$$\chi = \pi - 2\theta_m \tag{105}$$

Now the scattering angle can then be expressed in terms of the impact parameter, relative velocity and potential function.

$$\chi(b, g) = \pi - 2\int_{r_m}^{\infty} \frac{b}{r^2}\left[1 - \frac{b^2}{r^2} - \frac{2\phi(r)}{\mu g^2}\right]^{-\frac{1}{2}} dr \tag{106}$$

The expression for the scattering angle in (106) will be useful in determining the collision cross section for charged particle interactions.

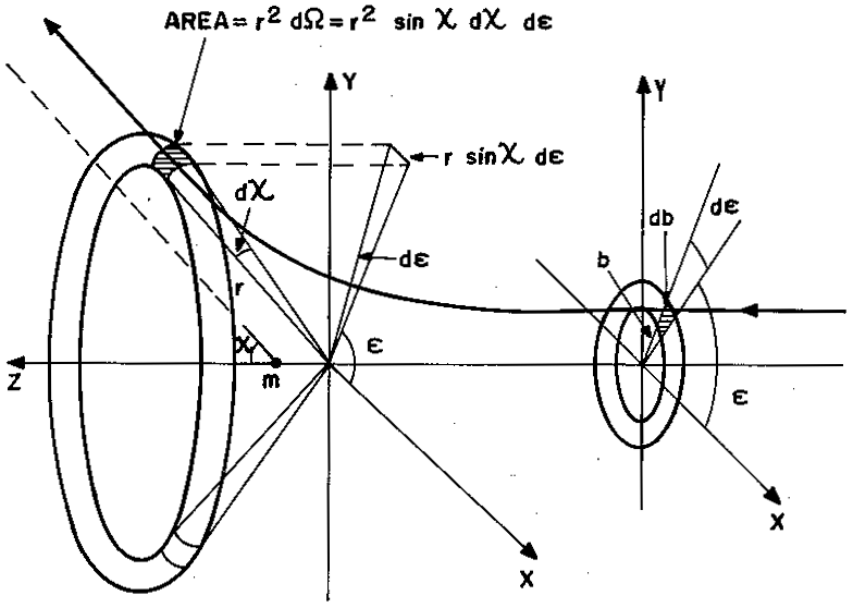

Figure 50: Differential Angles[6]

Figures 50 and 51 show the relevant differential areas for a particle interaction. Particles passing through the differential area $bdbd\epsilon$ are scattered through the area $r^2 d\Omega$. The rate at which particles are scattered will depend on the flux of incident particles. Figure 50 more closely illustrates the relationship between the impact parameter and scattering angle. The

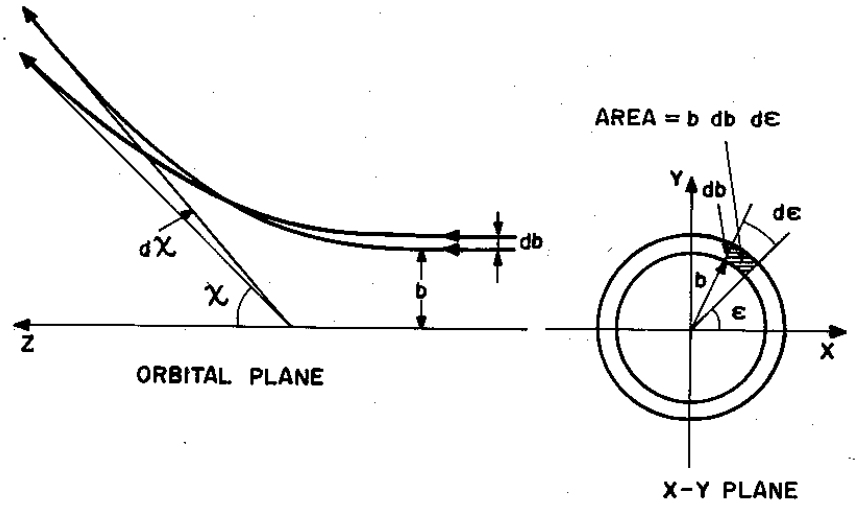

Figure 51: Differential Angles[6]

differential scattering cross section, or angular distribution function, is now introduced. The angular distribution function, $\sigma(\chi, \epsilon)$ is the number of particles scattered per second, per unit flux per unit area $d\Omega$. The number of particles scattered per second, dN/dt will be related to the collision frequency and collisionality regime.

$$\frac{dN}{dt} = \sigma(\chi, \epsilon)\Gamma d\Omega \tag{107}$$

Since particles passing through $d\Omega$ are the same particles that enter though $bdbd\epsilon$, the rate dN/dt can be expressed differently.

$$\frac{dN}{dt} = \Gamma bdbd\epsilon \tag{108}$$

Equating (107) and (108) and substituting $d\Omega = \sin\chi d\chi$, the angular distribution function is written in terms of b and χ.

$$\sigma(\chi, \epsilon) = \frac{b}{\sin\chi}\frac{db}{d\chi} \tag{109}$$

The transfer of momentum is the basic event that drives diffusion and mobility in a gas.[6].

The momentum cross section, σ_m, describes the rate of momentum transfer. The definition of the momentum cross section depends on the differential scattering cross section $\sigma(\chi, \epsilon)$

$$\sigma_m = \int_\Omega (1 - \cos\chi)\, \sigma(\chi, \epsilon) d\Omega \tag{110}$$

The definition of σ_m in equation(110) retains a dependency on the angle ϵ. It is assumed that the angular distribution of incident particles is uniform, and therefore the dependence on ϵ can be removed be integrating over all angles.

$$\sigma_m = 2\pi \int_{\chi_{min}}^{\pi} (1 - \cos\chi)\, \sigma(\chi) \sin\chi d\chi \tag{111}$$

The calculation of the momentum cross section for charged particle interaction, begins with a potential function, $\phi(r)$ for a coulomb interaction.

$$\phi(r) = \frac{1}{4\pi\epsilon_o} \frac{qq_1}{r} \tag{112}$$

The distance of closest approach, r_m is given by

$$r_m = \frac{b^2}{-b_o + \sqrt{b_o^2 + b^2}}, \quad \text{where} \quad b_o = \frac{qq_1}{4\pi\epsilon_o \mu g^2} \tag{113}$$

Integrating equation (106), yields

$$\tan\left(\frac{\chi}{2}\right) = \frac{b_o}{b} \tag{114}$$

Equation (114) is used to write an expression for b, which is differentiated and substituted into equation(109).

$$\frac{db}{d\chi} = \frac{b^2}{2b_o \cos^2\left(\frac{\chi}{2}\right)} \tag{115}$$

$$\sigma(\chi) = \frac{b_o^2}{(1 - \cos\chi)^2} \tag{116}$$

The result in equation (116) is substituted into equation(111).

$$\sigma_m = 2\pi b_o^2 \int_{\chi_{min}}^{\pi} \frac{\sin\chi}{1-\cos\chi} d\chi \tag{117}$$

The integration in equation(117) yields

$$\sigma_m = 4\pi b_o^2 \ln\left(\frac{1}{\sin(\chi_{min}/2)}\right) \tag{118}$$

At this point, $\chi_m in$ is still unknown. A cutoff value is imposed which corresponds to an impact parameter equal to the Debye length. This is an approximation for the effect of Debye screening as suggested by Bittencourt.[6]

$$\sigma_m = 2\pi b_o^2 \ln\left(1 + \left(\frac{\lambda_D}{b_o}\right)^2\right) \tag{119}$$

Equation (119) can be very well approximated assuming the Debye length is much larger than b_o, the impact parameter corresponding to a scattering angle of $\frac{\pi}{2}$.

$$\sigma_m = 4\pi b_o^2 \ln\left(\frac{\lambda_D}{b_o}\right) \quad \text{when } \lambda_D \gg b_o \tag{120}$$

The quantity b_o is dependent on the relative velocity g^2. In order to apply this method to calculate the mean free path of a gas, an average quantity must be used for g^2. Assuming a Maxwellian energy distribution, the average velocity is proportional to the temperature.[6]

$$\langle g^2 \rangle = \frac{3kT}{\mu} \tag{121}$$

The mean free path can then be calculated based on the momentum cross section.

$$\lambda = \frac{1}{\sigma_m n} \tag{122}$$